Electronic Supplementary Information (ESI)

Improving the Cd^{2+} sensing capability of a new anionic Rare Earth Metal-Organic Framework based on a $[RE_6(\mu_3\text{-}OH)_8]^{10+}$ secondary building unit: An ion - exchange approach towards more efficient sensors

Nikos Panagiotou[a], Kasiani Evangelou[a], Athanasia Psalti[b], Nektaria Varnava[a], Giasemi K. Angeli[c], Pantelis N. Trikalitis[c], John C. Plakatouras[ad], Theodore Lazarides[b]*, Anastasios J. Tasiopoulos[a]*

[a]Department of Chemistry, University of Cyprus, 1678 Nicosia, Cyprus. E-mail: atasio@ucy.ac.cy

[b]Laboratory of Inorganic Chemistry, Department of Chemistry, Aristotle University of Thessaloniki, 54124 Thessaloniki, Greece. E-mail: tlazarides@chem.auth.gr

[c]Department of Chemistry, University of Crete, Voutes 71003, Heraklion, Greece.

[d]On sabbatical leave from Department of Chemistry, University of Ioannina, 45110 Ioannina, Greece.

Table of Contents

Experimental Section

Photoluminescence Measurements and Cadmium Sensing Studies. Steady state emission and excitation spectra and the decay profiles for $((CH_3)_2NH_2)^+_2$(**1**)$(Y_{0.95}Eu_{0.05})$ and $((CH_3)_2NH_2)^+_2$(**1**)$(Y_{0.95}Tb_{0.05})$ were measured using an Edinburgh Xe900 spectrofluorometer. Solid state excitation spectra (excitation and emission slit = 2.5nm) were measured by monitoring the emission intensity at 404nm (for H_2OBA, $((CH_3)_2NH_2)^+_2$(**1**)(Y) and the Na^+ - and Mg^{2+} - exchanged analogues), at 614nm (for $((CH_3)_2NH_2)^+_2$(**1**)$(Y_{0.95}Eu_{0.05})$ and at 543nm (for $((CH_3)_2NH_2)^+_2$(**1**)$(Y_{0.95}Tb_{0.05})$ and emission spectra (excitation and emission slit = 2.5nm) were recorded with an excitation wavelength of 311nm and 351nm (for $((CH_3)_2NH_2)^+_2$(**1**)(Y) and the Na^+ - and Mg^{2+} - exchanged analogues) and 311 nm for $((CH_3)_2NH_2)^+_2$(**1**)$(Y_{0.95}Eu_{0.05})$ and$((CH_3)_2NH_2)^+_2$(**1**)$(Y_{0.95}Tb_{0.05})$.

Fluorescence titration studies for both the $((CH_3)_2NH_2)^+_2$(**1**)$(Y_{0.95}Eu_{0.05})$ and the Na_2(**1**)$(Y_{0.95}Eu_{0.05})$ materials was conducted after suspension of the corresponding crystals in DMF. More precisely, 1 mg of crystals was transferred in a vial containing 10 ml DMF and a fine suspension formed after sonication of the mixture for 1 h. Fluorescence titrations were conducted by adding an aqueous solution of Cd^{2+} ions (solution of $CdCl_2$ 10^{-2} M) in the sample to be measured, by increments of 5 μl, 10 μl and 20 μl, successively. Regeneration experiments were performed by addition to a fine suspension of Na_2(**1**)$(Y_{0.95}Eu_{0.05})$ in DMF (0.1 mg/ mL) formed after sonication of the mixture for 1 h, an aqueous solution of $CdCl_2$ (10^{-2} M) by increments of 5 μl, 10 μl and 20 μl, successively followed by addition of aliquots of saturated aqueous solution of NaCl. After each addition the luminescence spectra were recorded with λ_{ex} = 283nm.

Single crystal X-ray crystallography. Single Crystal X-ray diffraction data were collected on a Rigaku Supernova A diffractometer, equipped with a CCD area detector utilizing Cu-Kα (λ = 1.5418 Å) radiation. A suitable crystal was mounted on a Hampton cryoloop with Paratone-N oil and transferred to a goniostat where it was cooled for data collection. The structures were solved by direct methods using SHELXT and refined on F^2 using full-matrix least squares using SHELXL14.1.[1] Software packages used: CrysAlis CCD for data collection, CrysAlis RED for cell refinement and data reduction[2], WINGX for geometric calculations[3], and DIAMOND for molecular graphics[4]. The non-H atoms were treated anisotropically, whereas the aromatic

hydrogen atoms were placed in calculated, ideal positions and refined as riding on their respective carbon atoms. Electron density contributions from disordered guest molecules and dimethyl ammonium ions were handled using the SQUEEZE procedure from the PLATON software suit[5] due to the disordered nature of these ions. Selected crystal data for $((CH_3)_2NH_2)^+_2$(**1**)(Y) and $((CH_3)_2NH_2)^+_2$(**1**)(Ho) are summarized in Table S1. CCDC 1971376 ($((CH_3)_2NH_2)^+_2$(**1**)(Y) and 1971377 $((CH_3)_2NH_2)^+_2$(**1**)(Ho) contains the supplementary crystallographic data for this paper. Full details can be found in the CIF files provided as Supplementary Information.

Table S1. Selected Crystal Data for $((CH_3)_2NH_2)^+_2$(**1**)(Y) and $((CH_3)_2NH_2)^+_2$(**1**)(Ho).

Empirical formula	$C_{42}H_{24}O_{19}Y_3$	$C_{48}H_{48}N_3O_{22}Ho_3$
Formula weight	1099.34	1513.68
Temperature	104.8(6) K	109(7) K
Wavelength	1.54184 Å	1.54184 Å
Crystal system	Trigonal	Trigonal
Space group	$R\bar{3}$	$R\bar{3}$
Unit cell dimensions	a = 27.755(2) Å, α = 90° b = 27.755(2) Å, β = 90° c = 24.566(4) Å, γ = 120°	a = 27.765(1) Å, α = 90° b = 27.765(1) Å, β = 90° c = 24.633(1) Å, γ = 120°
Volume	16389(3) $Å^3$	16445.2(16) $Å^3$
Z	6	6
Density (calculated)	0.668 g/cm^3	0.917 g/cm^3
Absorption coefficient	2.360 mm^{-1}	4.220 mm^{-1}
F(000)	3270	4404
Crystal size	0.061 x 0.054 x 0.018 mm^3	0.046 x 0.044 x 0.026 mm^3
θ range for data collection	4.042 to 66.995°	4.033 to 67.000°
Index ranges	-30<=h<=25, -22<=k<=33, -29<=l<=29	-33<=h<=33, -25<=k<=33, -29<=l<=26
Reflections collected	11775	30299
Independent reflections	6482 [R_{int} = 0.0327]	6540 [R_{int} = 0.0412]
Completeness to θ = 66.995°	99.5%	99.9%
Refinement method	Full-matrix least-squares on F^2	Full-matrix least-squares on F^2
Data / restraints / parameters	6482 / 0 / 193	6540 / 0 / 222
Goodness-of-fit	1.030	1.061
Final R indices [I > 2σ(I)]	R_{obs} = 0.0880, wR_{obs} = 0.2608	R_{obs} = 0.0602, wR_{obs} = 0.1838
R indices [all data]	R_{all} = 0.1076, wR_{all} = 0.2739	R_{all} = 0.0741, wR_{all} = 0.1934
Largest diff. peak and hole	1.654 and -1.122 $e·Å^{-3}$	1.450 and -0.883 $e·Å^{-3}$

[a]$R = \Sigma||F_o|-|F_c|| / \Sigma|F_o|$, $wR = \{\Sigma[w(|F_o|^2 - |F_c|^2)^2] / \Sigma[w(|F_o|^4)]\}^{1/2}$ and
[b]$w=1/[\sigma^2(F_o^2)+(mP)^2+nP]$ where $P=(Fo^2+2Fc^2)/3$ and m and n are constants.

Gas sorption measurements. Low Pressure gas sorption measurements were carried out at different temperatures using an Autosorb-iQ2 by Quantachrome equipped with a cryocooler system capable of temperature control from 20 to 320K. Prior to analysis the as made samples were washed with N,N- dimethylformamide four times per day for 1 day and then soaked in dichloromethane (DCM) 5 times per day for 5 days. Finally, the DCM exchanged samples were activated using supercritical CO_2, weighted accurately and transferred to the analysis port of the gas sorption instrument.

Cadmium sorption measurements. Cadmium sorption experiments were performed at room temperature (296 ± 2K) under normal atmospheric conditions in DMF/H_2O (7:3) solutions. The preparation of the test solutions involved dilution of an appropriate amount of a Cd^{2+} stock solution (0.1 M) that was prepared by dissolution of $CdCl_2 \cdot 6H_2O$ in distilled water. Generally, test solutions (30 ml) containing Cd^{2+} of known concentration, were mixed with a given mass of MOF and the resulting suspension was shaken in a thermostated orbital shaker (at 100 rpm) for 2 h to assure that equilibrium had been reached. For studying the effect of initial Cd^{2+} concentration, the latter was varied between 10^{-5} and $9*10^{-3}$ M in the test suspensions (0.033g of MOF in 30 ml solution). For kinetic studies certain amount of MOF (0.033 g) was mixed with 100 ml of Cd^{2+} solution ($[Cd^{2+}] = 1*10^{-3}$ M, T = 296 K for $((CH_3)_2NH_2)^+_2$(**1**)(Y) and the metal concentration was determined at regular time steps. For the Cd^{2+} analysis, aliquots collected from the suspension were filtered with membrane filters (pore size: 0.22 μm) and the Cd^{2+} concentration was determined with ICP-OES.

Physical Measurements/Characterization

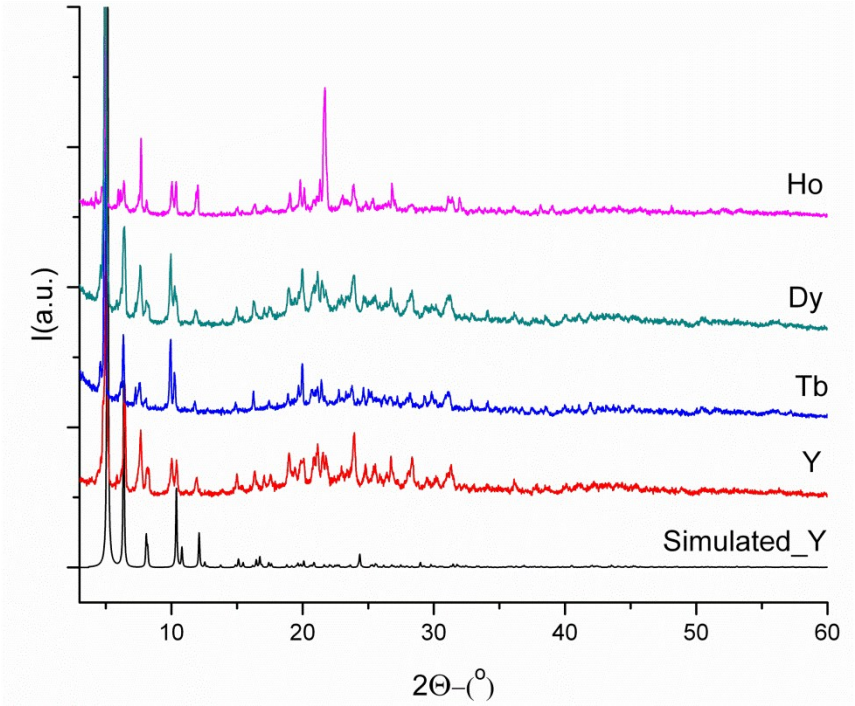

Figure S1. Powder X-ray diffraction pattern of the as synthesized compounds $((CH_3)_2NH_2)^+_2$(**1**)(RE), along with the simulated pattern of $((CH_3)_2NH_2)^+_2$(**1**)(Y) from the single crystal data.

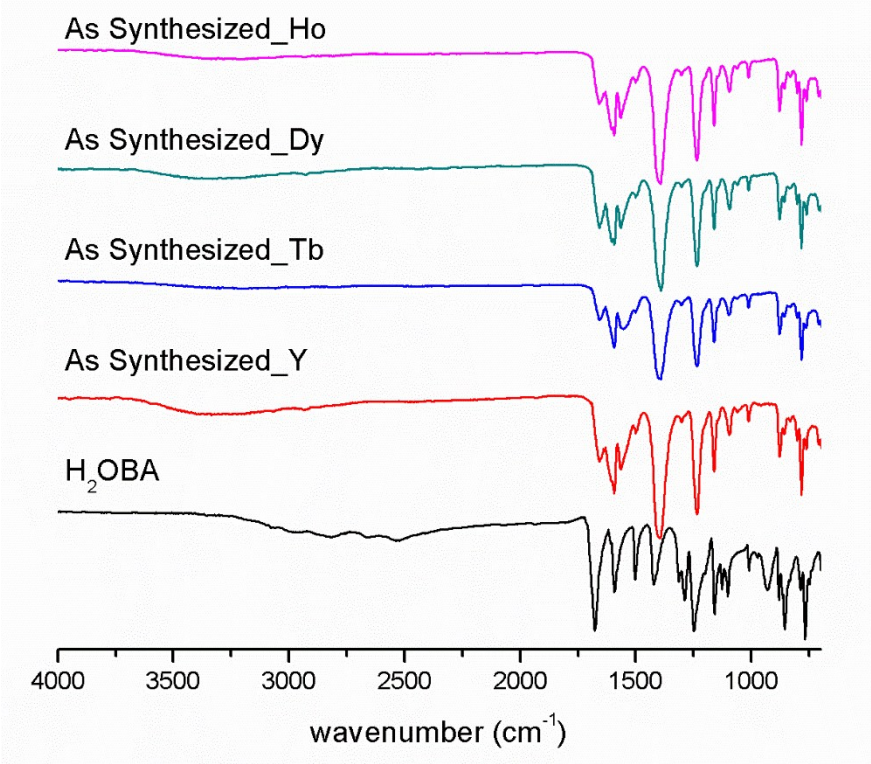

Figure S2. IR spectra of H_2OBA and the as synthesized compounds $((CH_3)_2NH_2)^+_2$(**1**)(RE).

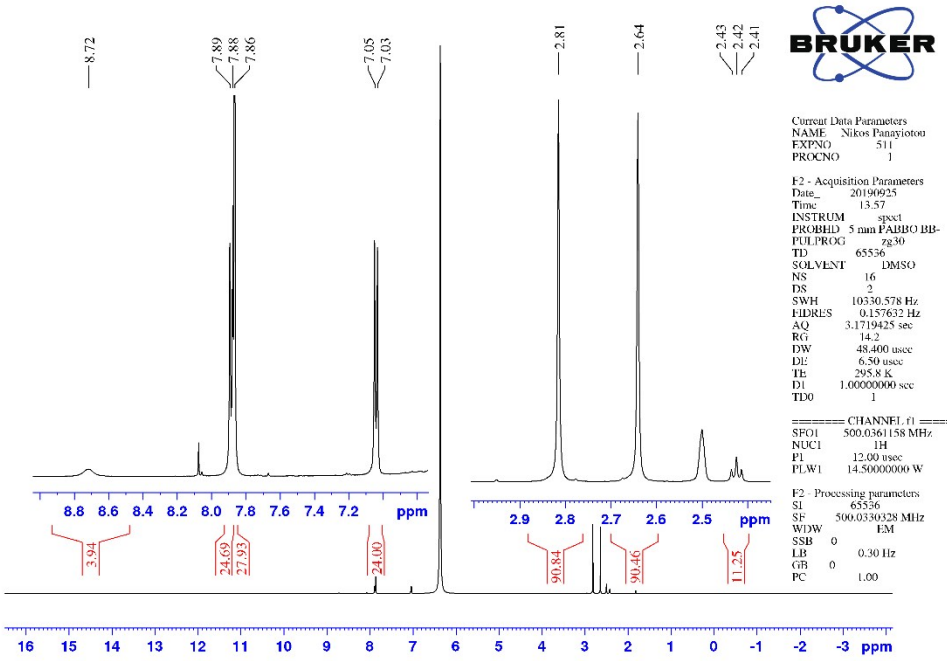

Figure S3. ^{1}H-NMR spectrum of as synthesized $((CH_3)_2NH_2)^+_2$(**1**)(Y) digested in 25μL of concentrated HCl in d_6-DMSO. These data indicate the presence of the organic ligand OBA^{2-} as well as $2(CH_3)NH_2^+$ and DMF molecules in $((CH_3)_2NH_2)^+_2$(**1**)(Y). ^{1}H NMR (d_6-DMSO): δ 2.42 (t, 6H, C**H$_3$**, $2((CH_3)NH_2^+)$), δ 2.5 (q, 6H, residual solvent peaks), δ 2.64 (s, 3H, C**H$_3$**, DMF), δ 2.81 (s, 3H, C**H$_3$**, DMF), δ 7.04 (d, 4H, Ar-**H**, OBA^{2-}), δ 7.86 (s, H, C**HO**, DMF), δ 7.88 (d, 4H, Ar-**H**, OBA^{2-}), δ 8.72 (bs, 4H, N**H$_2$**, $2((CH_3)NH_2^+)$).

Topological Analysis

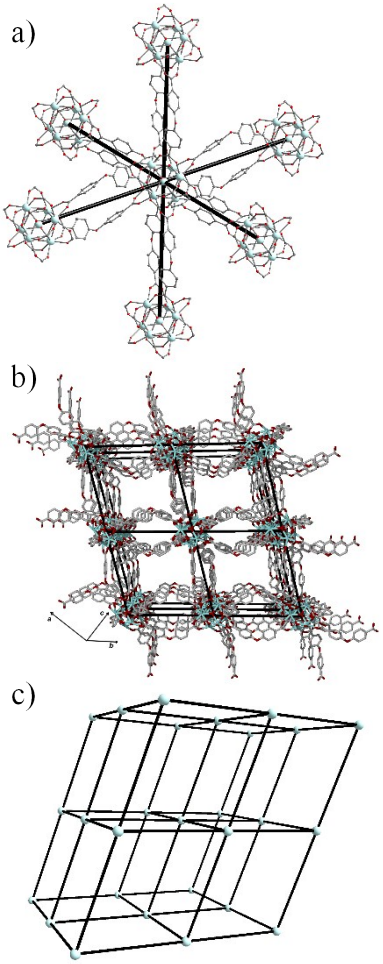

Figure S4. Topological analysis of $((CH_3)_2NH_2^+)_2$(**1**)(RE) a) A pair of OBA^{2-} ligands representing a single linkage between SBUs b) Representation of the interconnection between the SBUs in the 3D framework showing the underlying **pcu** topology. c) **pcu** topology of the $((CH_3)_2NH_2^+)_2$(**1**)(RE). Color code: Y, light blue; O, red; C, grey.

Stability Studies

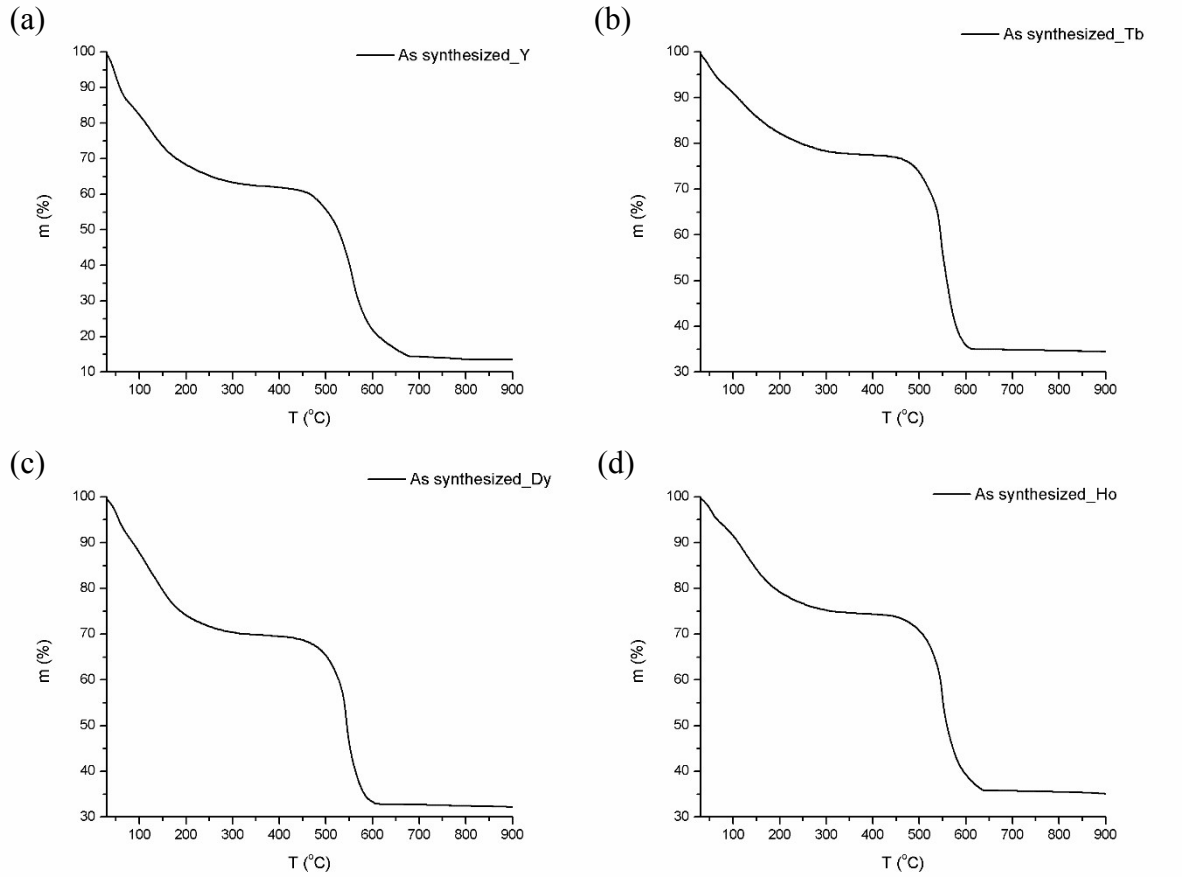

Figure S5. TGA graphs of the as synthesized compounds $((CH_3)_2NH_2)^+_2$(**1**)(RE) ((a) RE = Y, (b) RE = Tb, (c) RE = Dy, (d) RE = Ho). TG analysis reveals that the thermal decomposition of compounds $((CH_3)_2NH_2)^+_2$(**1**)(RE) proceeds via a two-step process. The first step (until ~470°C) is attributed to the removal of the lattice DMF molecules. The second mass loss which is completed at ~700°C for $((CH_3)_2NH_2)^+_2$(**1**)(Y) and at ~650°C for ($((CH_3)_2NH_2)^+_2$(**1**)(RE); RE = Tb, Dy, Ho) is attributed to the decomposition of the ligand OBA^{2-}. Lastly the residual mass at 900°C corresponds to the rare earth oxide of the corresponding RE^{III} ion. Details on calculated values for solvent removal and ligand decomposition along with the experimental values obtained from TG analysis are shown in Table S2.

Table S2. Calculated values for solvent removal and ligand combustion along with the experimental values obtained from TG analysis for the as synthesized compounds $((CH_3)_2NH_2)^+_2$(**1**)(RE)

Compound $((CH_3)_2NH_2)^+_2$(**1**)(RE)	Lattice Solvent Removal			Ligand and $(CH_3)_2NH_2^+$ Combustion		Residual Oxide		
	Temperature (°C)	Experimental (Calculated) (%)	xDMF	Temperature (°C)	Experimental (Calculated) (%)	Temperature (°C)	Experimental (Calculated) (%)	Formula
$((CH_3)_2NH_2)^+_2$(**1**)(Y)·xDMF	470	40 (40.2)	21	700	44 (42.5)	900	16 (17.8)	Y_2O_3
$((CH_3)_2NH_2)^+_2$(**1**)(Tb)·xDMF	470	25 (25)	12.5	650	40 (39)	900	35 (31)	Tb_4O_7
$((CH_3)_2NH_2)^+_2$(**1**)(Dy)·xDMF	470	30 (31)	17	650	38.5 (41)	900	31.5 (28)	Dy_2O_3
$((CH_3)_2NH_2)^+_2$(**1**)(Ho)·xDMF	470	25 (25.5)	13	650	41 (44)	900	34 (30.5)	Ho_2O_3

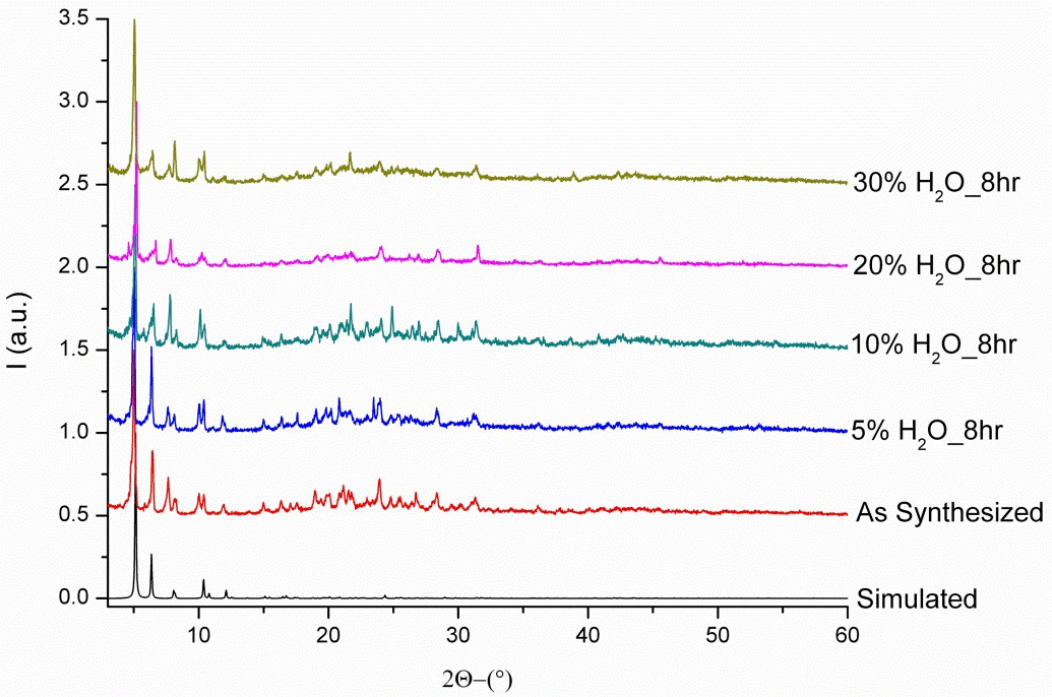

Figure S6. Powder X-ray diffraction patterns of as synthesized $((CH_3)_2NH_2)^+_2$(**1**)(Y) treated (as described in the experimental part) in the aqueous DMF solutions for 8hrs.

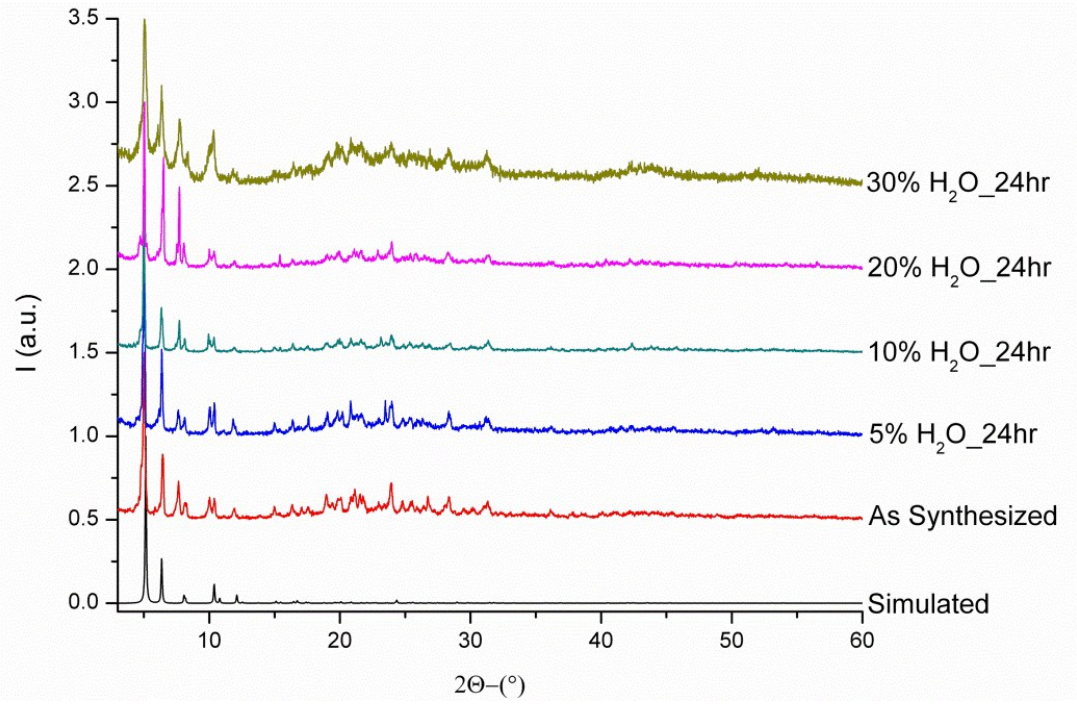

Figure S7. Powder X-ray diffraction patterns of as synthesized $((CH_3)_2NH_2)^+_2$(**1**)(Y) treated (as described in the experimental part) in the aqueous DMF solutions for 24hrs.

Characterization of Na^+- and Mg^{2+} - exchanged analogues

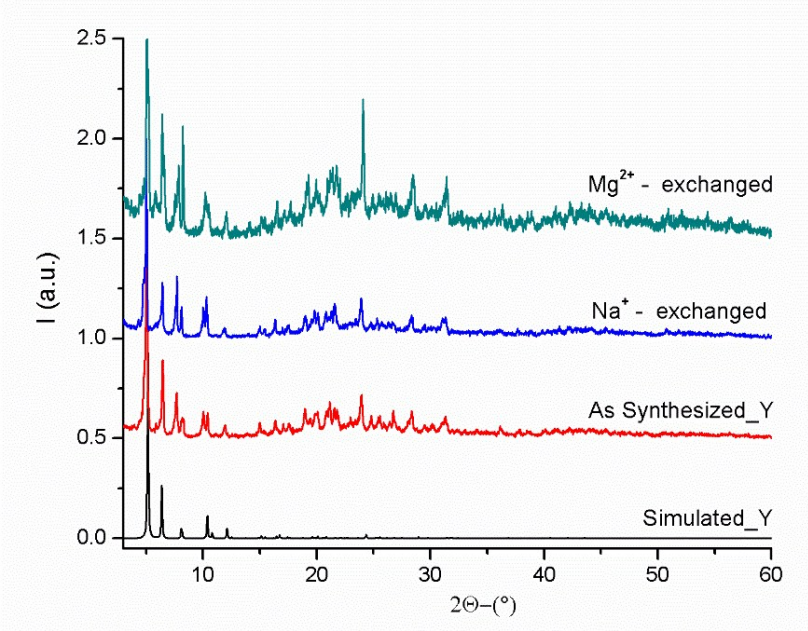

Figure S8. Powder X-ray diffraction patterns of $((CH_3)_2NH_2)^+_2$(**1**)(Y) treated (as described in the experimental part) with a 0.5M DMF solution of the corresponding metal nitrate salt indicated in the figure.

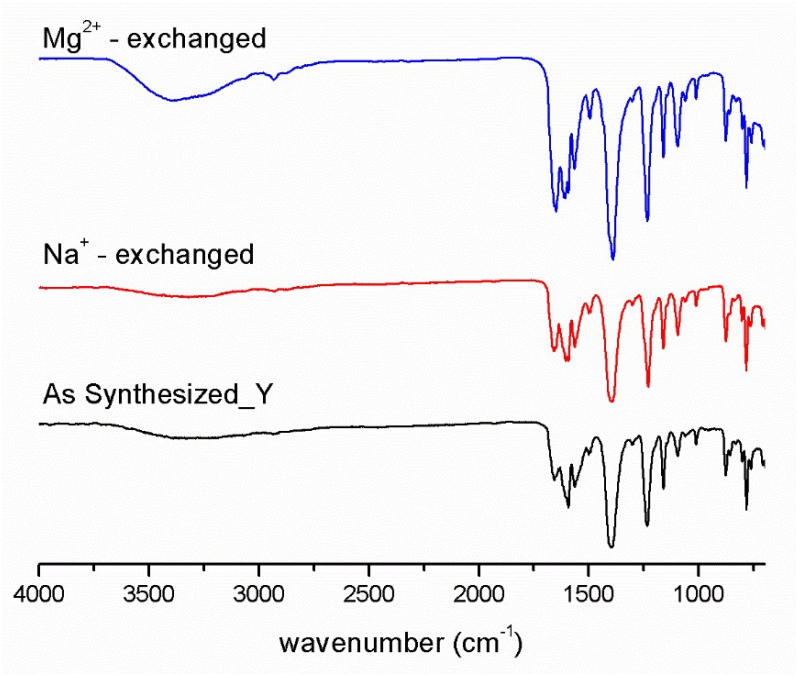

Figure S9. IR spectra of $((CH_3)_2NH_2)^+_2$(**1**)(Y) treated (as described in the experimental part) with a 0.5M DMF solution of the corresponding metal nitrate salt indicated in the figure.

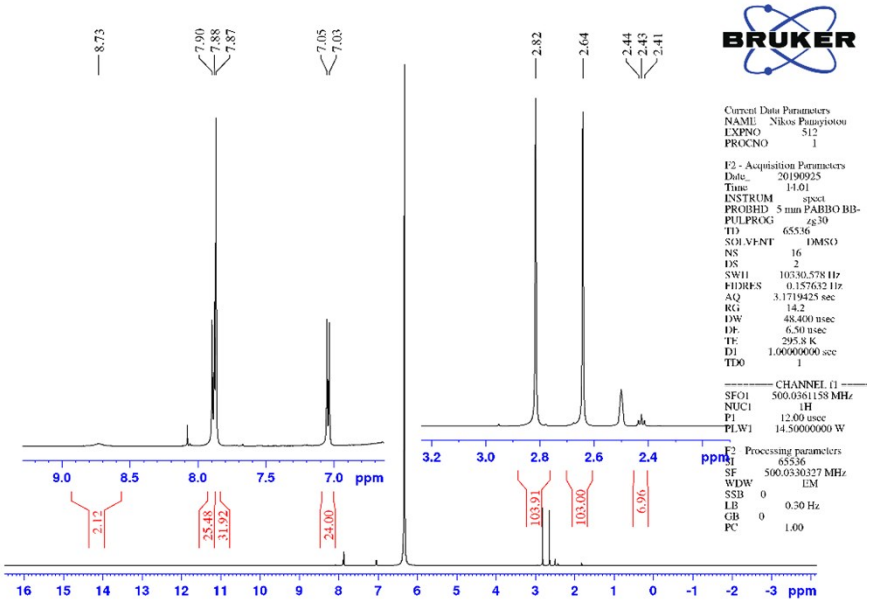

Figure S10. ^{1}H-NMR spectrum of $((CH_3)_2NH_2)^+_2$(**1**)(Y) crystals after partial exchange of the $(CH_3)NH_2^+$ ions with Na^+ digested in 25μL concentrated HCl in d_6-DMSO. These data indicate the presence of the organic ligand OBA^{2-} as well as DMF and $((CH_3)NH_2^+$ in $(\mathbf{1})(Y)^{2-}$ although the latter are partially replaced by Na^+ ions as revealed by the integration of the ^{1}H-NMR peaks assigned to $((CH_3)NH_2^+$ which is decreased compared to the corresponding one of the pristine material shown in Fig. S4. Exact assignment of the ^{1}H-NMR peaks is given in Figure S4.

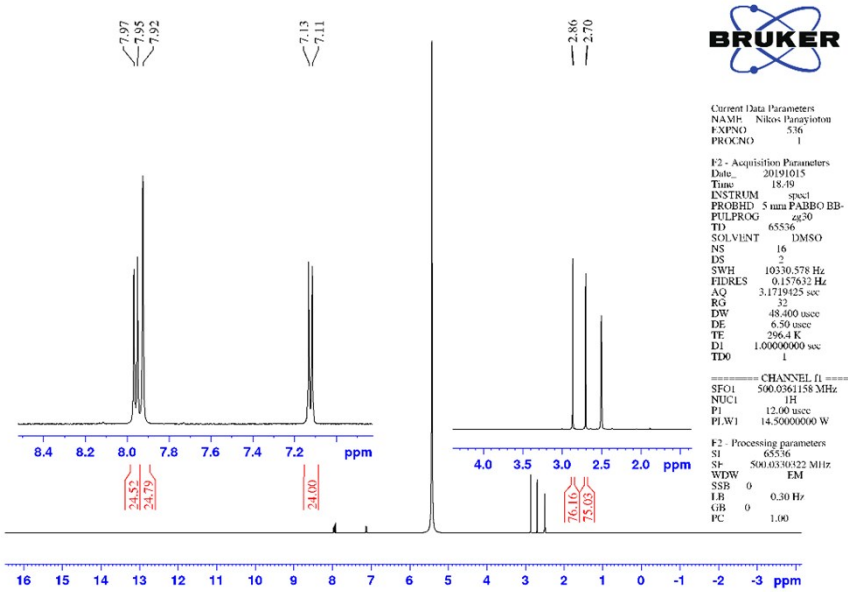

Figure S11. ^{1}H-NMR spectrum of Na_2(**1**)(Y) digested in 25μL concentrated HCl in d_6-DMSO. These data indicate the presence of the organic ligand OBA^{2-} and DMF in $(\mathbf{1})(Y)^{2-}$ and the absence of $((CH_3)_2NH_2)^+$ which is completely replaced by Na^+. Exact assignment of the OBA^{2-} and DMF ^{1}H-NMR peaks is given in Figure S4.

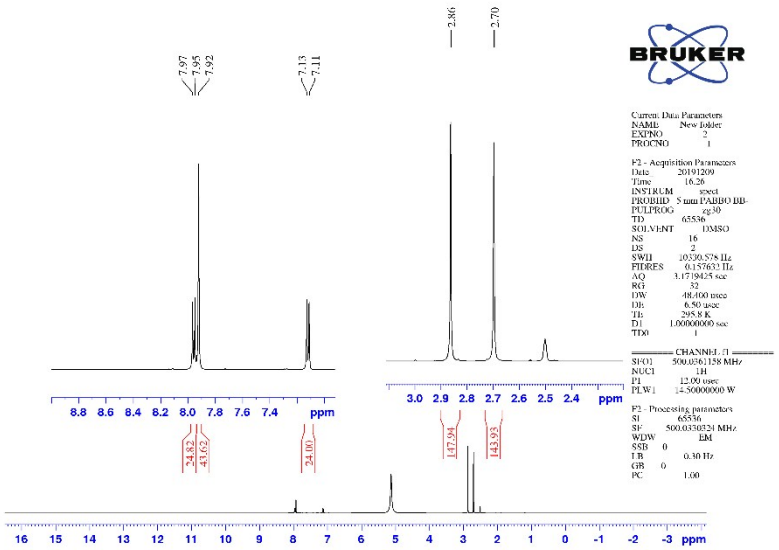

Figure S12. ^{1}H-NMR spectrum of Mg(**1**)(Y) digested in 25µL concentrated HCl in d_6-DMSO. These data indicate the presence of the organic ligand OBA^{2-} and DMF in $(\mathbf{1})(Y)^{2-}$ and the absence of $((CH_3)_2NH_2)^+$ which is completely replaced by Mg^{2+}. Exact assignment of the OBA^{2-} and DMF ^{1}H-NMR peaks is given in Figure S4.

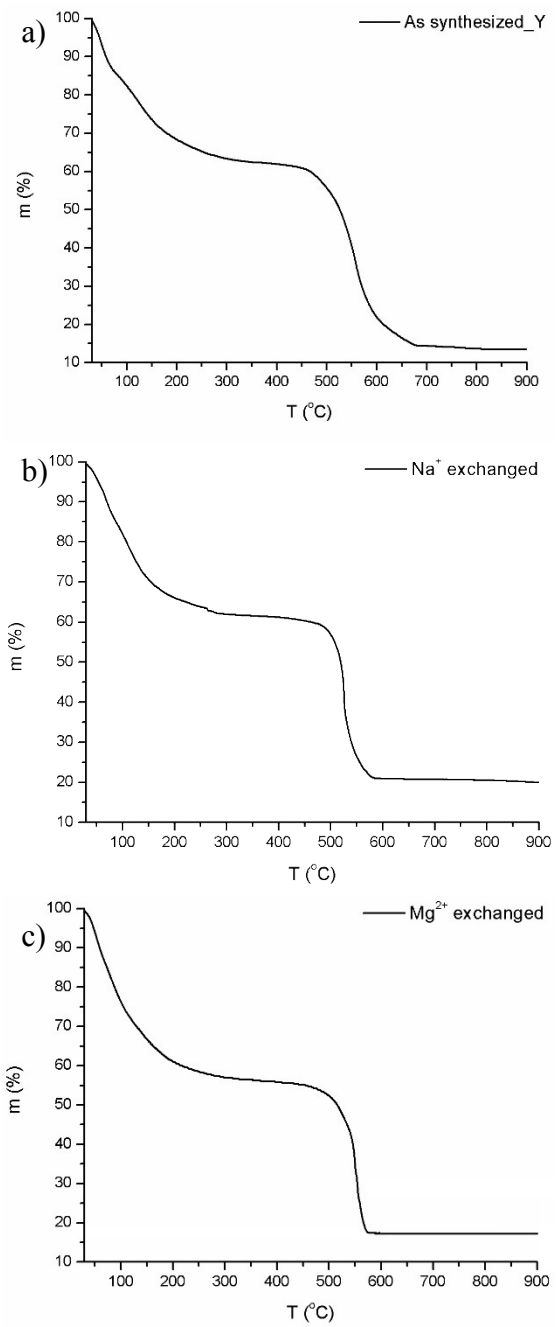

Figure S13. TGA curves of the Na^+ - and Mg^{2+} - exchanged analogues and in particular of (a) $((CH_3)_2NH_2)^+_2$(**1**)(Y), (b) Na_2(**1**)(Y) and (c) Mg(**1**)(Y). TG analysis reveals that the thermal decomposition of compounds Na_2(**1**)(Y) and Mg(**1**)(Y) proceeds via a two-step process. The first step (until ~470°C) is attributed to the removal of the lattice DMF molecules. The second mass loss which is completed at ~700°C for $((CH_3)_2NH_2)^+_2$(**1**)(Y) and at ~600°C for two exchanged analogues is attributed to the decomposition of the ligand OBA^{2-}. Lastly the residual mass at 900°C corresponds to the mixed oxide of Y_2O_3/Na_2O or Y_2O_3/MgO. Details on calculated values for solvent removal and ligand combustion along with the experimental values obtained from TG analysis are listed in Table S3.

Table S3. Calculated values for solvent removal and ligand combustion along with the experimental values obtained from TG analysis for the as synthesized compound $((CH_3)_2NH_2)^+_2$(**1**)(Y) and the exchanged analogues Na_2(**1**)(Y) and Mg(**1**)(Y).

$M_{(2/n)}$(**1**)(Y)	Lattice Solvent Removal			Ligand Combustion		Residual Oxide		
	Temperature (°C)	Experimental (Calculated) (%)	xDMF	Temperature (°C)	Experimental (Calculated) (%)	Temperature (°C)	Experimental (Calculated) (%)	Formula
$((CH_3)_2NH_2)^+_2$(**1**)(Y)·xDMF	470	40 (40.2)	21	700	44 (42.5)	900	16 (17.8)	Y_2O_3
Na_2(**1**)(Y)·xDMF	470	40 (40)	20.5	600	39 (40)	900	21 (20)	$Y_2O_3 \cdot Na_2O$
Mg(**1**)(Y)·xDMF	470	45 (45.4)	22	600	37.5 (36.7)	900	17.5 (17.3)	$Y_2O_3 \cdot MgO$

Gas Sorption Measurements

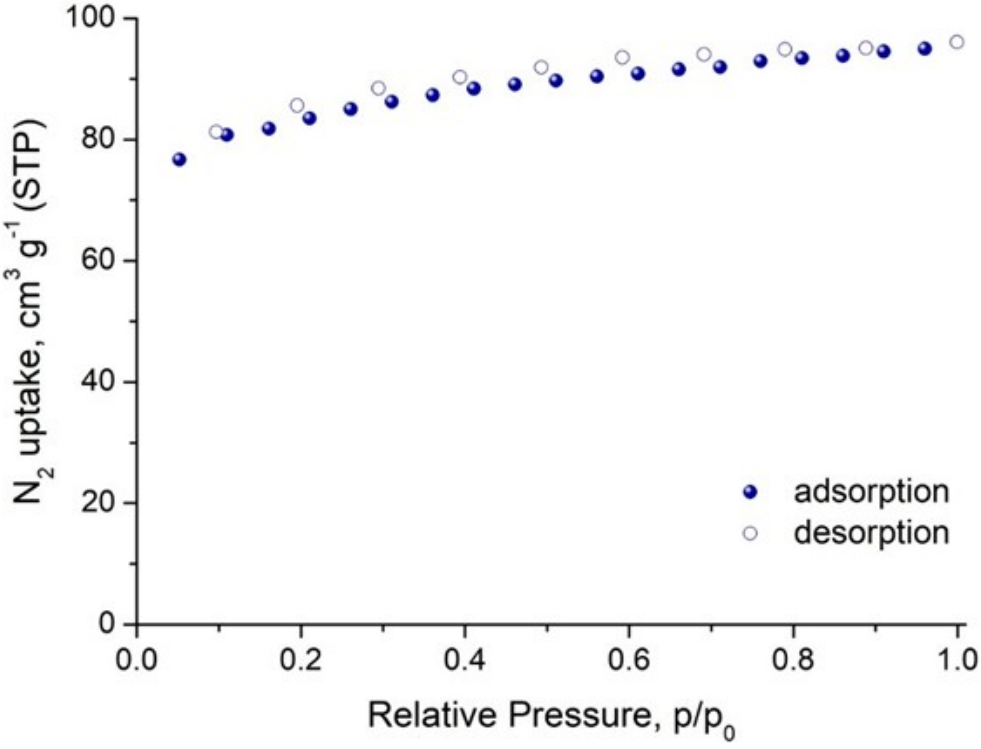

Figure S14. N_2 adsorption isotherm of $((CH_3)_2NH_2)^+_2$(**1**)(Y) recorded at 77 K.

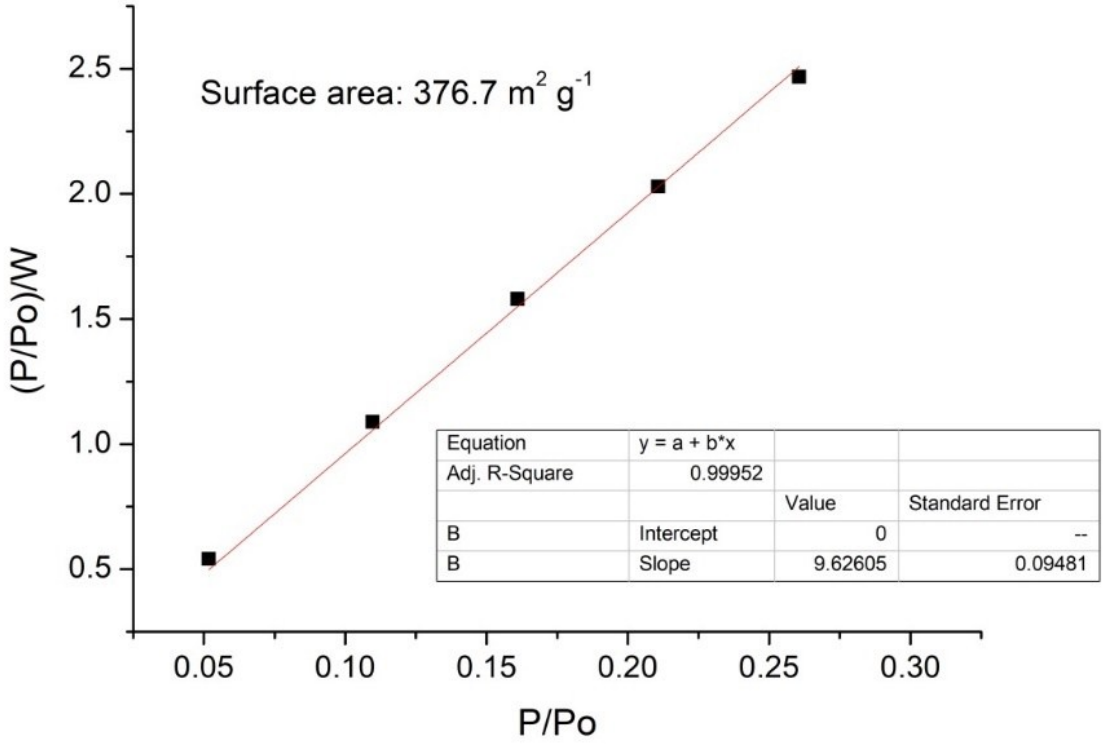

Figure S15. Langmuir plot for $((CH_3)_2NH_2)^+_2$(**1**)(Y) from N_2 adsorption isotherm at 77K.

Low pressure CO_2, sorption isotherms, determination of heat of adsorption.

Heat of adsorption: To calculate heats of adsorptions, the corresponding adsorption isotherms at two different temperatures (77 K / 87 K for H_2 and 273 K / 293 K for CO_2 and CH_4) were simultaneously fitted using the virial type[6,7] Equation 1:

$$\ln P = \ln N + \frac{1}{T}\sum_{i=0}^{m} a_i N^i + \sum_{i=0}^{n} b_i N^i \qquad (1)$$

The heat of adsorption at zero coverage was calculated from Equation 2, where as a function of surface coverage, from Equation 3:

$$Q_{st} = -Ra_o \qquad (2)$$

$$Q_{st}(N) = -R\sum_{i=0}^{m} a_i N^i \qquad (3)$$

For the determination of the isosteric heat of adsorption using the Clausious - Clapeyron equation a commercially available software, ASiQwin (version 3.01) purchased from Quantachrome, was used.

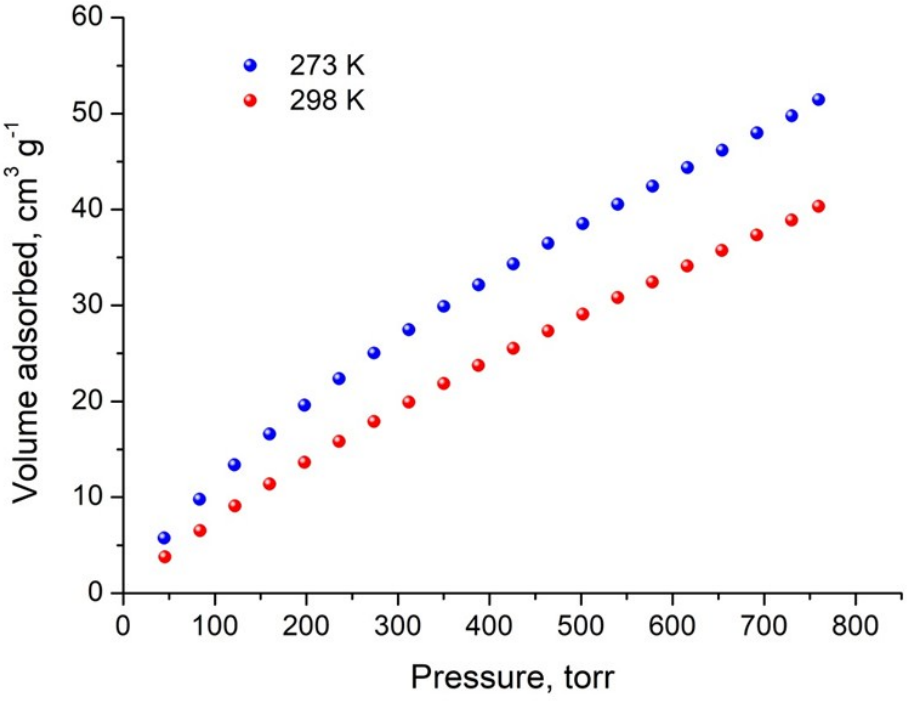

Figure S16. CO_2 adsorption isotherms of $((CH_3)_2NH_2)^+_2$(**1**)(Y) at 273 K and 298 K.

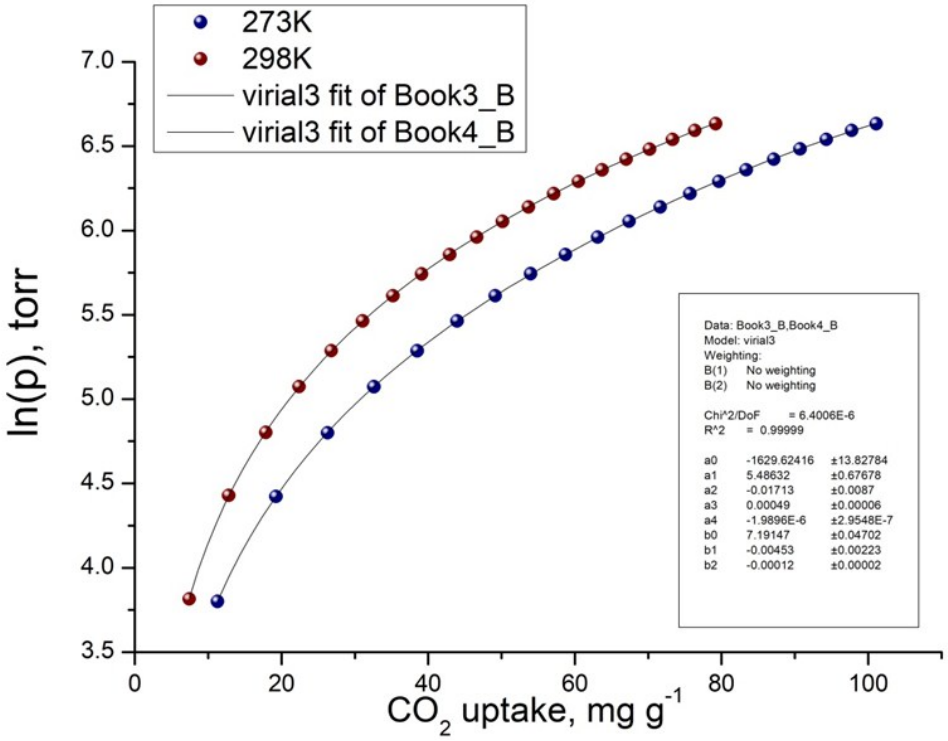

Figure S17. Virial type fitting of CO_2 adsorption isotherms of $((CH_3)_2NH_2)^+_2$(**1**)(Y) at 273 K, and 298 K according to equation 1.

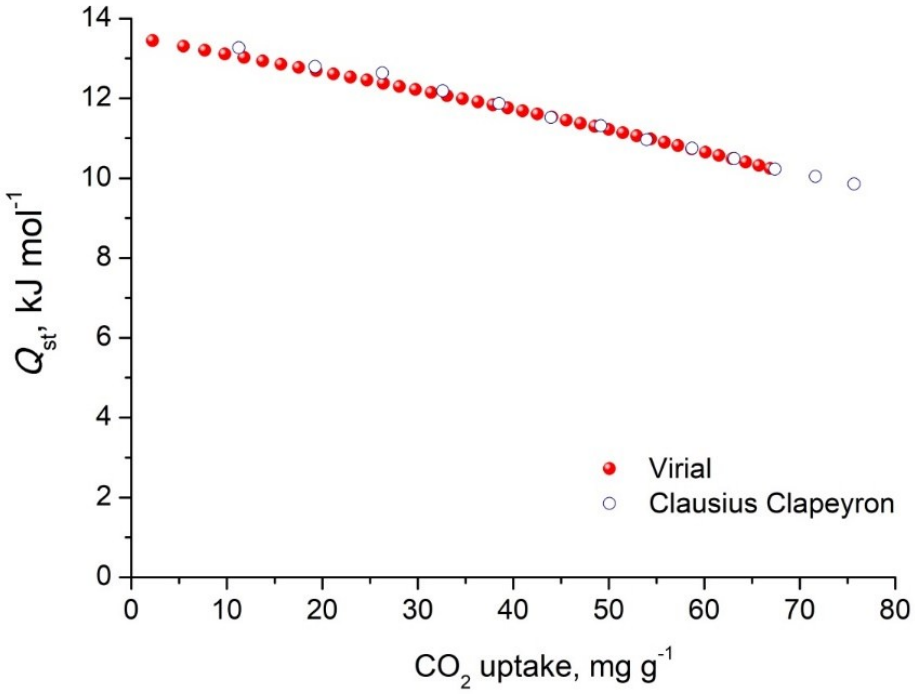

Figure S18. CO_2 isosteric heat of adsorption in $((CH_3)_2NH_2)^+_2$(**1**)(Y) as a function of surface coverage.

Photoluminescence Studies

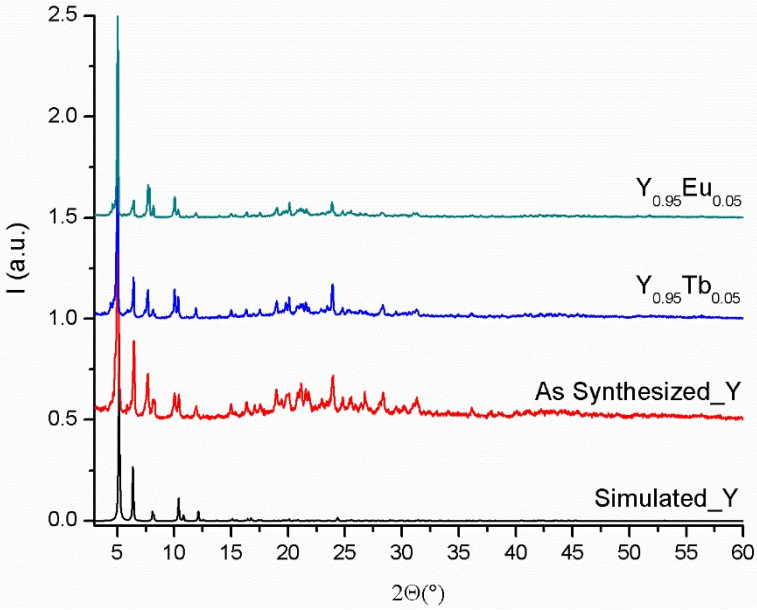

Figure S19. Powder X-ray diffraction patterns of the compound $((CH_3)_2NH_2)^+_2$(**1**)(Y) and doped analogues $((CH_3)_2NH_2)^+_2$(**1**)$(Y_{0.95}Eu_{0.05})$ and $((CH_3)_2NH_2)^+_2$(**1**)$(Y_{0.95}Tb_{0.05})$ along with the simulated pattern from the single crystal data.

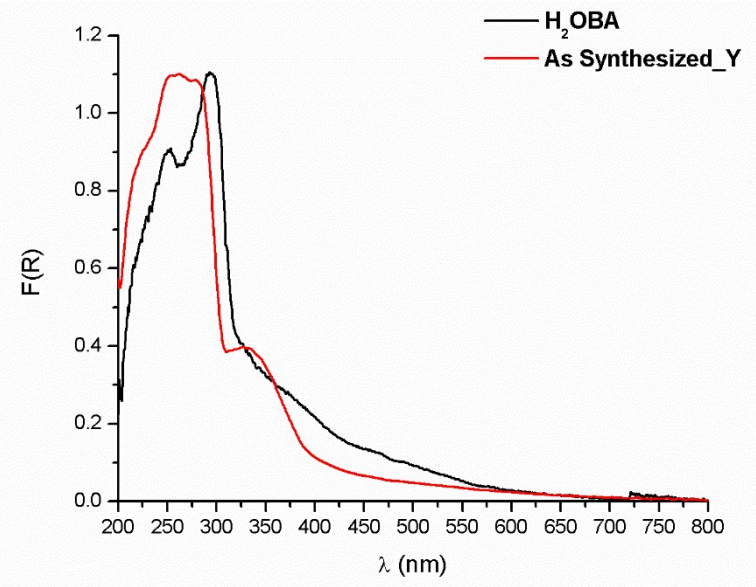

Figure S20. Solid state UV-Vis spectra recorded at room temperature of H_2OBA and the as synthesized compound $((CH_3)_2NH_2)^+_2$(**1**)(Y).

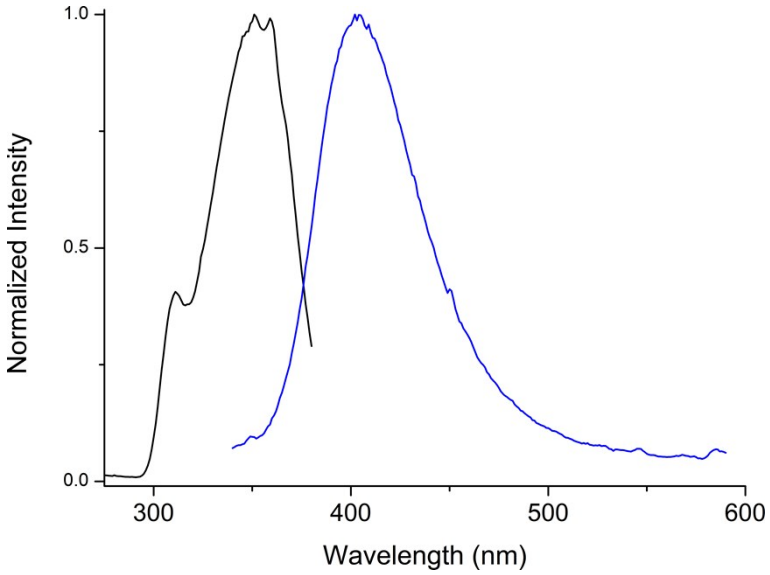

Figure S21. The emission (λ_{exc} = 310 nm) and excitation spectra of $((CH_3)_2NH_2)^+_2$(**1**)(Y).

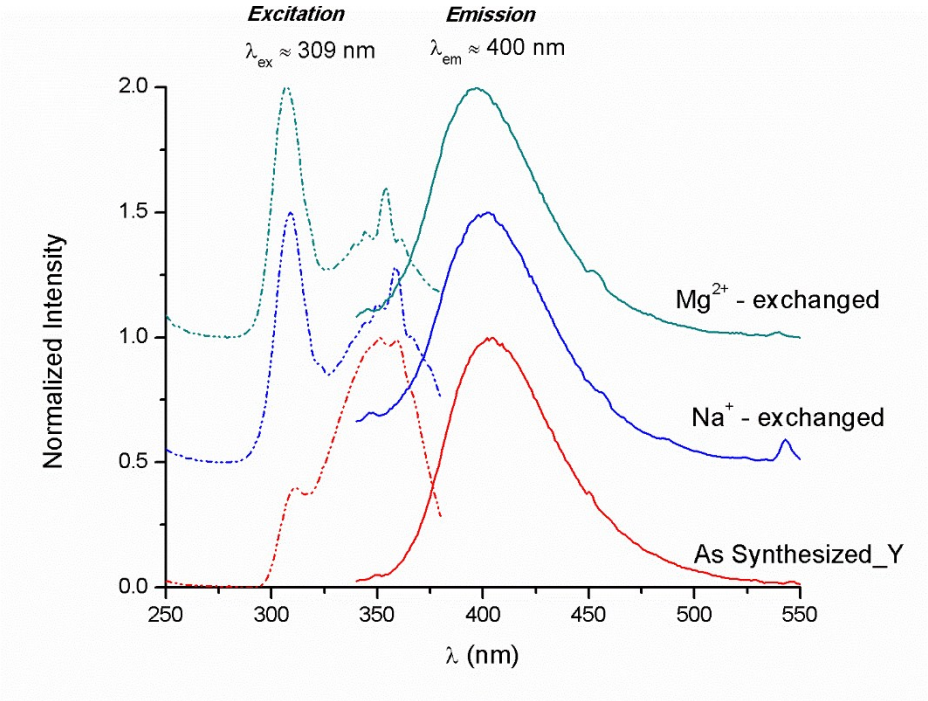

Figure S22. Solid state excitation ($\lambda_{em.}$ = 404nm) and emission ($\lambda_{exc.}$ = 311nm) at room temperature of $((CH_3)_2NH_2)^+_2$(**1**)(Y) and the exchanged analogues Na_2(**1**)(Y) and Mg(**1**)(Y).

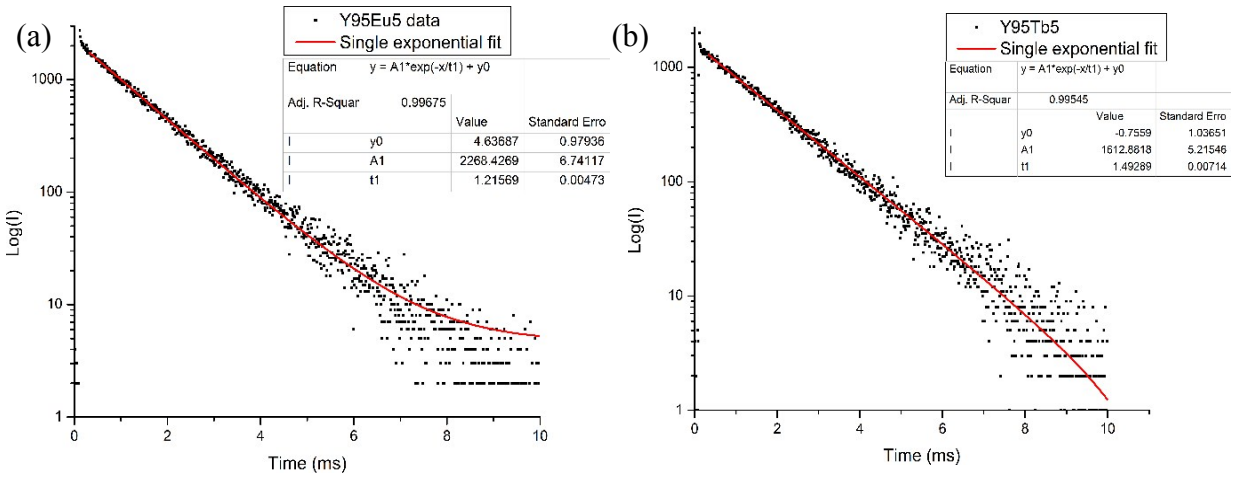

Figure S23. The decay of a) $((CH_3)_2NH_2)^+_2$(**1**)($Y_{0.95}Eu_{0.05}$) and b) $((CH_3)_2NH_2)^+_2$(**1**)($Y_{0.95}Tb_{0.05}$).

Cadmium/Mercury Sensing Studies

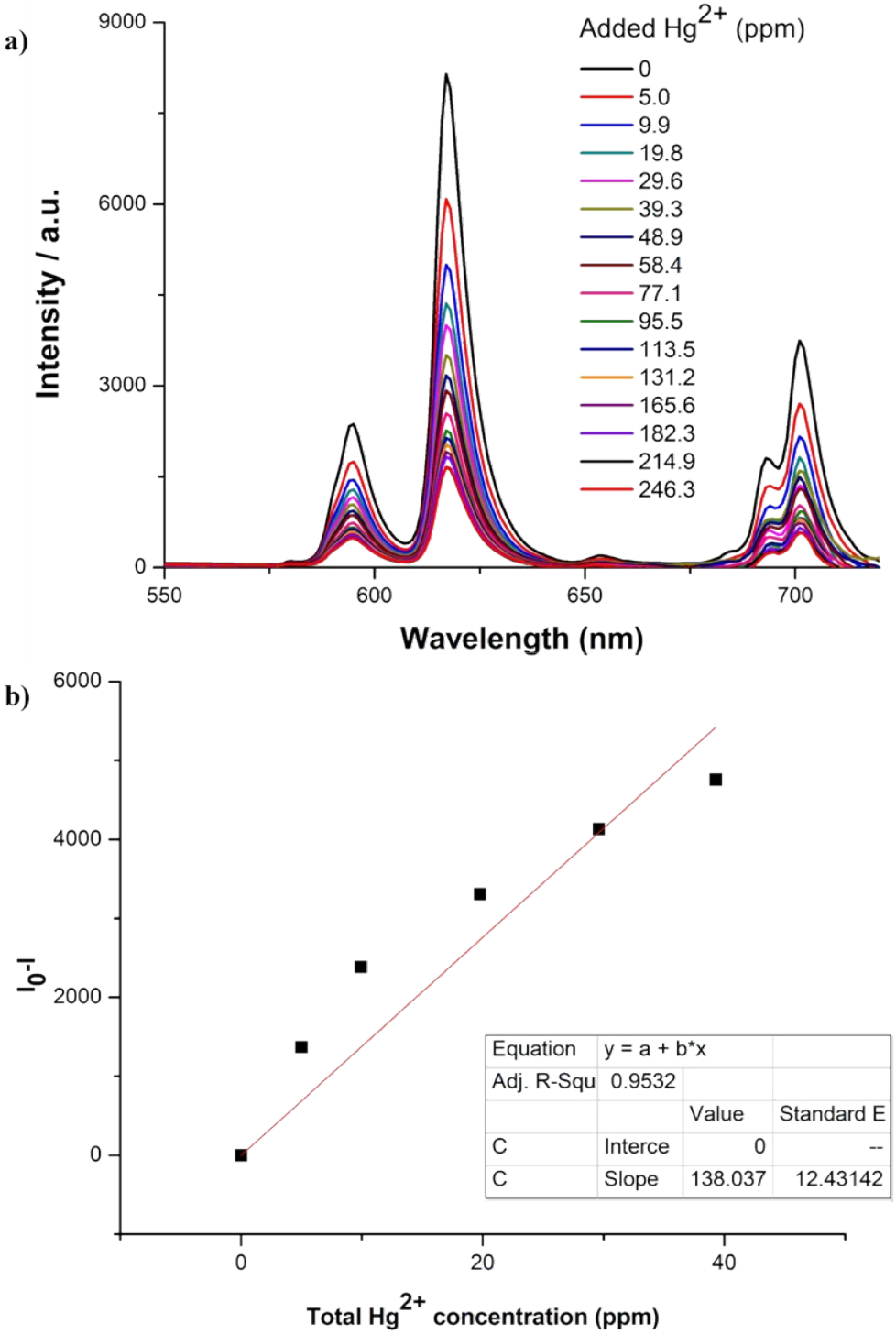

Figure S24. a) Luminescence titration of exchanged Na_2(**1**)($Y_{0.95}Eu_{0.05}$) suspended in DMF upon gradual addition of a 10^{-2} M aqueous solution of $HgCl_2$. b) Calibration curve of the titration of a DMF suspension of Na_2(1)($Y_{0.95}Eu_{0.05}$) with Hg^{2+}.

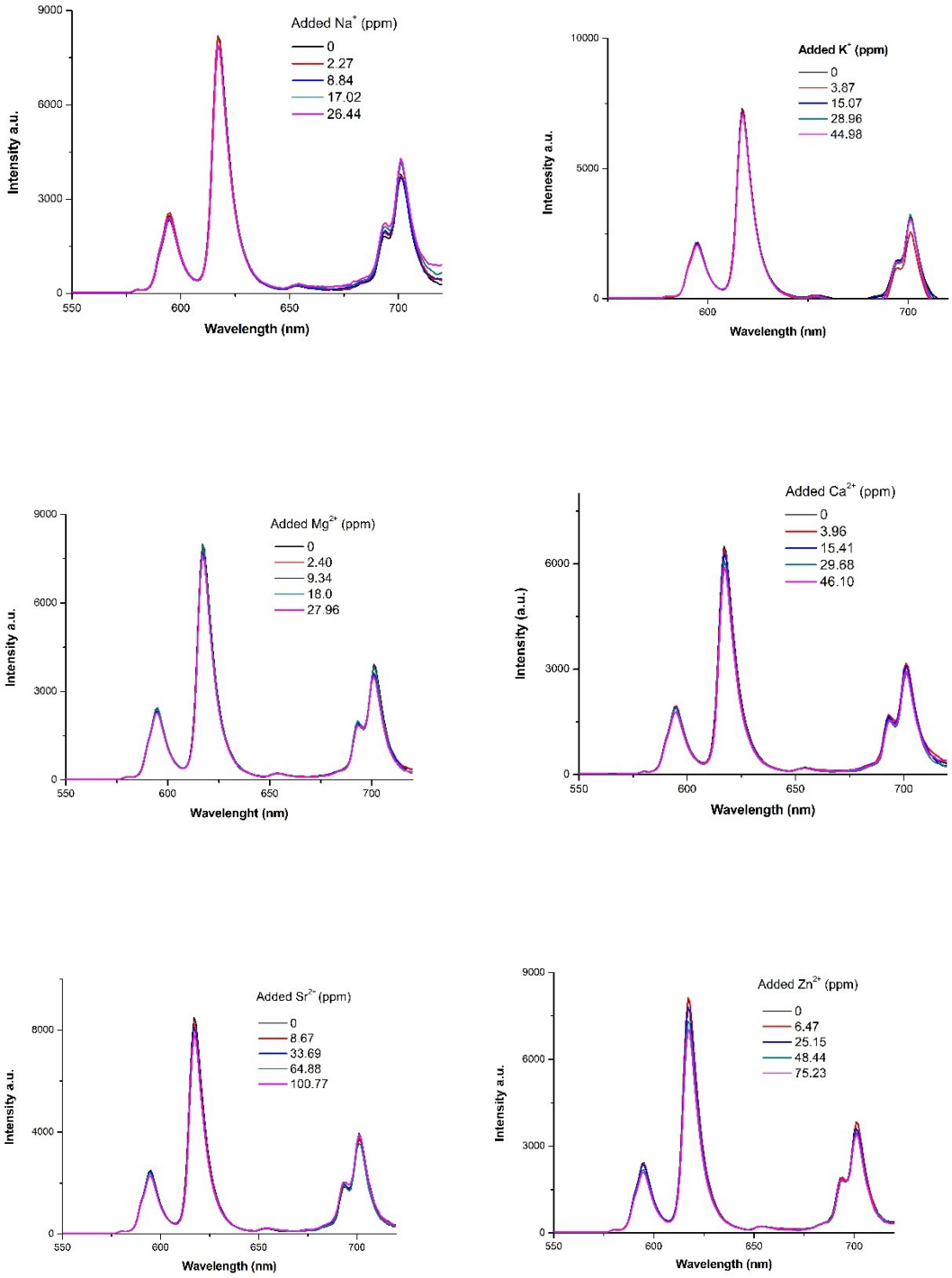

Figure S25. Results of control fluorescence titrations of DMF suspensions of Na_2(**1**)($Y_{0.95}Eu_{0.05}$) upon addition of aqueous solutions (10^{-2} M) of Na^+, K^+, Mg^{2+}, Ca^{2+}, Sr^{2+} and Zn^{2+}.

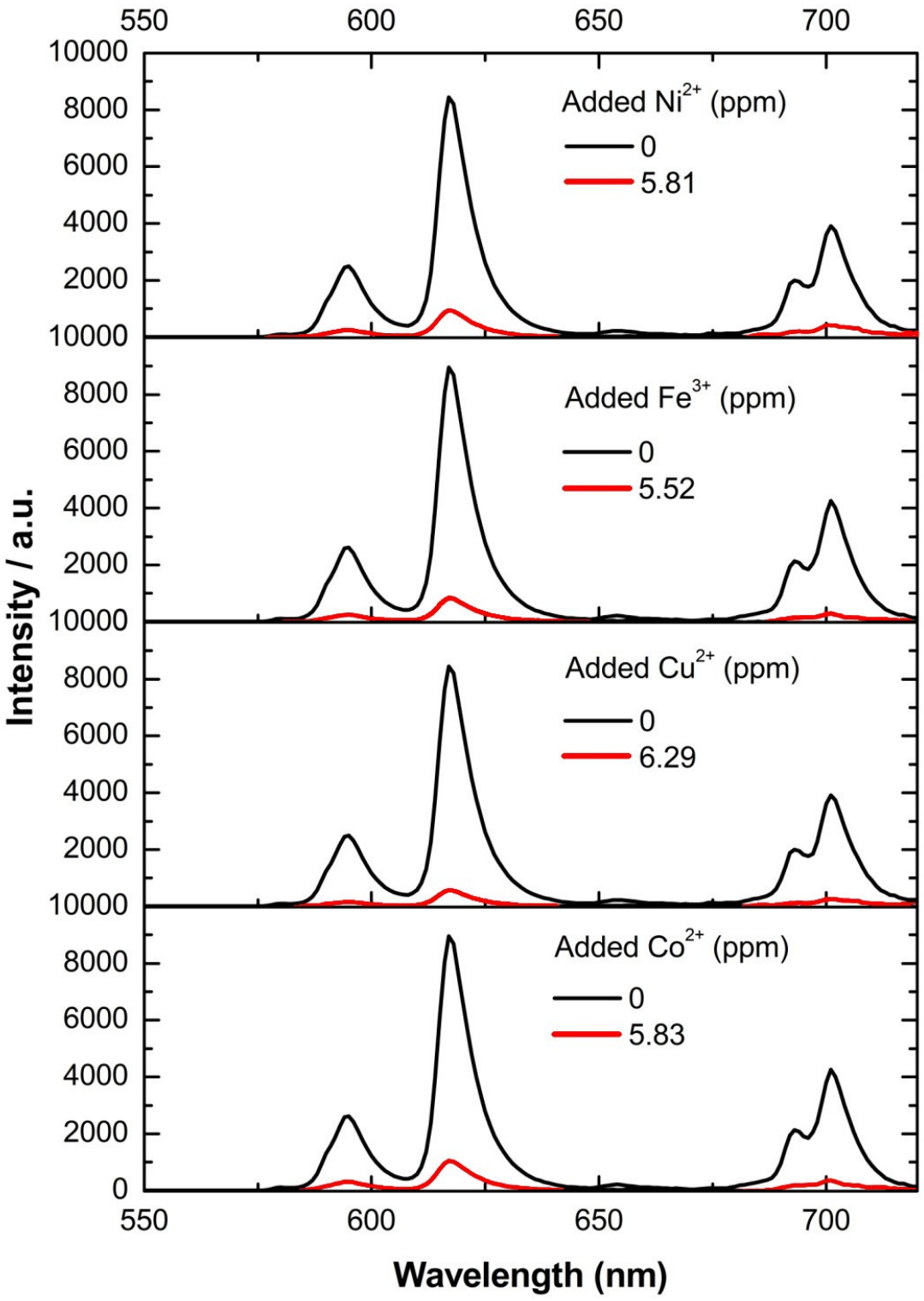

Figure S26. Quenching of the Eu^{3+} luminescence of Na_2(**1**)($Y_{0.95}Eu_{0.05}$) after addition of 20 µL of 10^{-2} M solutions of Ni^{2+}, Fe^{3+}, Cu^{2+} and Co^{2+}salts.

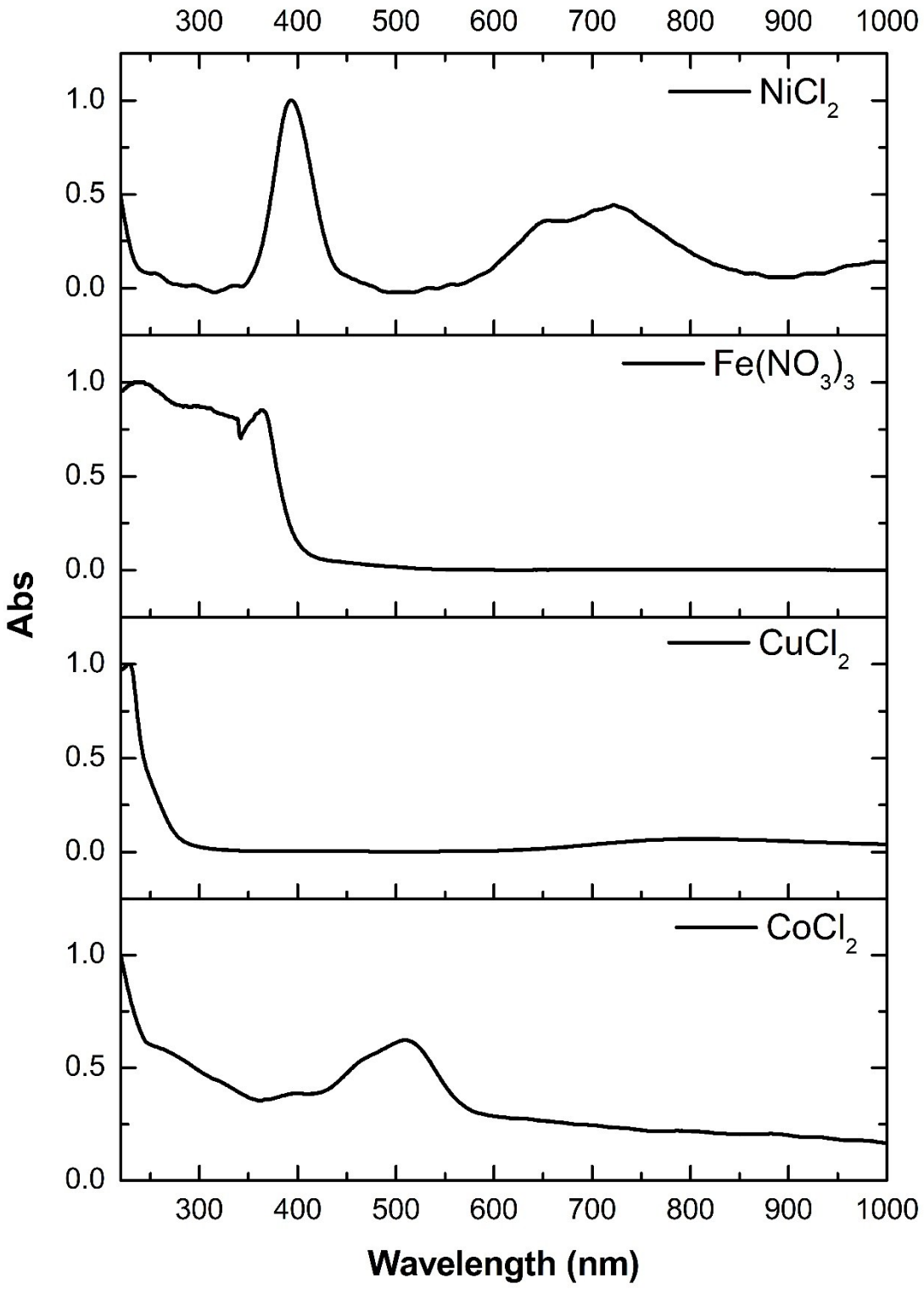

Figure S27. UV-vis absorption spectra of the 10^{-2} M stock aqueous solutions of Ni^{2+}, Fe^{3+}, Cu^{2+} and Co^{2+}.

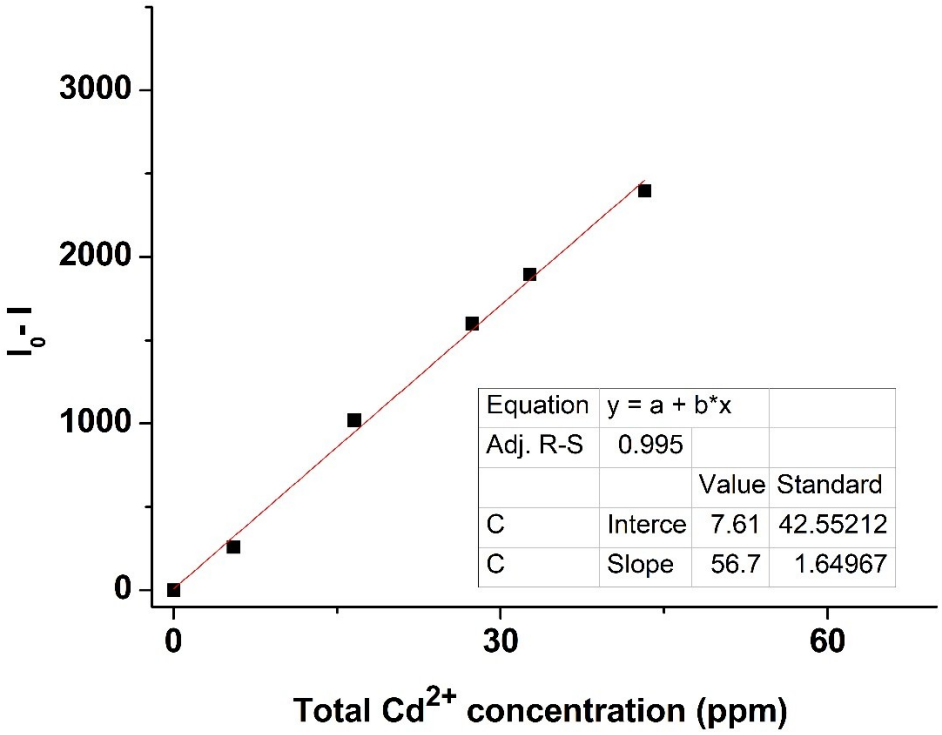

Figure S28. Calibration curve of the titration of a DMF suspension of $((CH_3)_2NH_2)^+_2$(**1**)($Y_{0.95}Eu_{0.05}$) with Cd^{2+}.

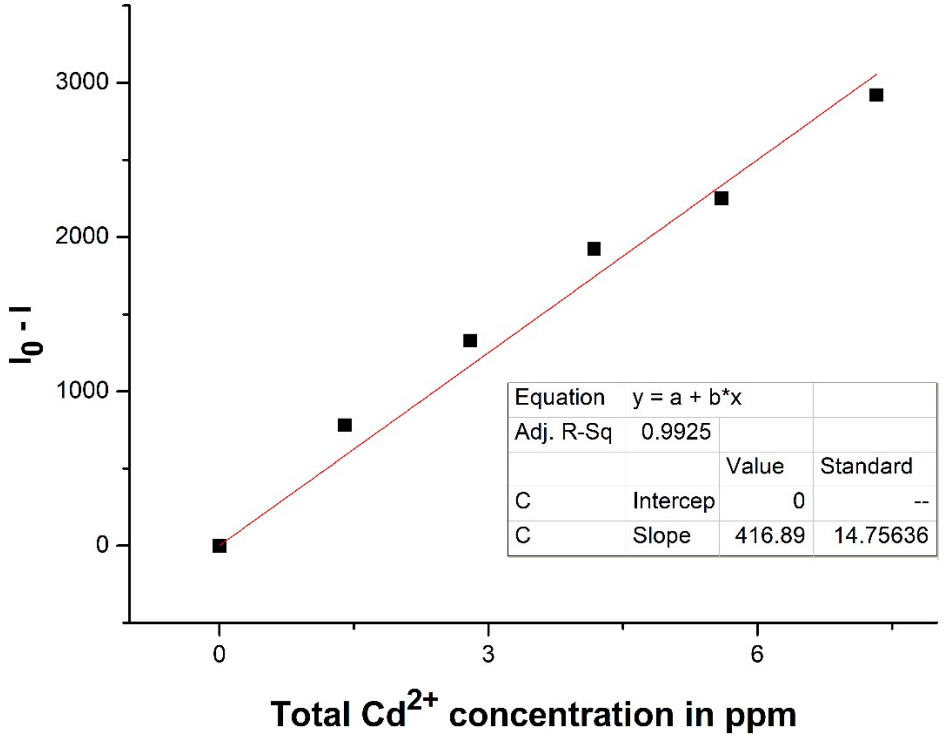

Figure S29. Calibration curve of the titration of a DMF suspension of Na_2(**1**)($Y_{0.95}Eu_{0.05}$) with Cd^{2+}.

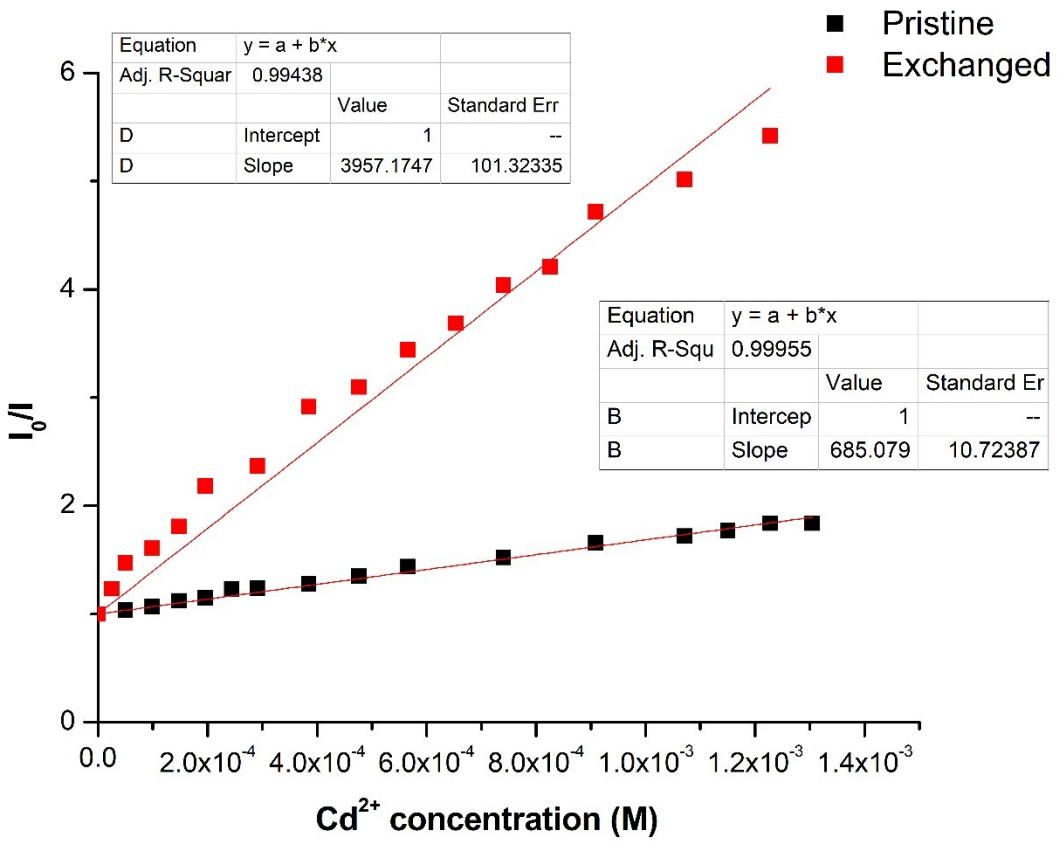

Figure S30. Stern-Volmer plots for $((CH_3)_2NH_2)^+_2$(**1**)$(Y_{0.95}Eu_{0.05})$ (black squares) and Na_2(**1**)$(Y_{0.95}Eu_{0.05})$ (red squares) and the corresponding linear fits indicated as solid lines.

Regeneration of Na_2@(1)(Y)

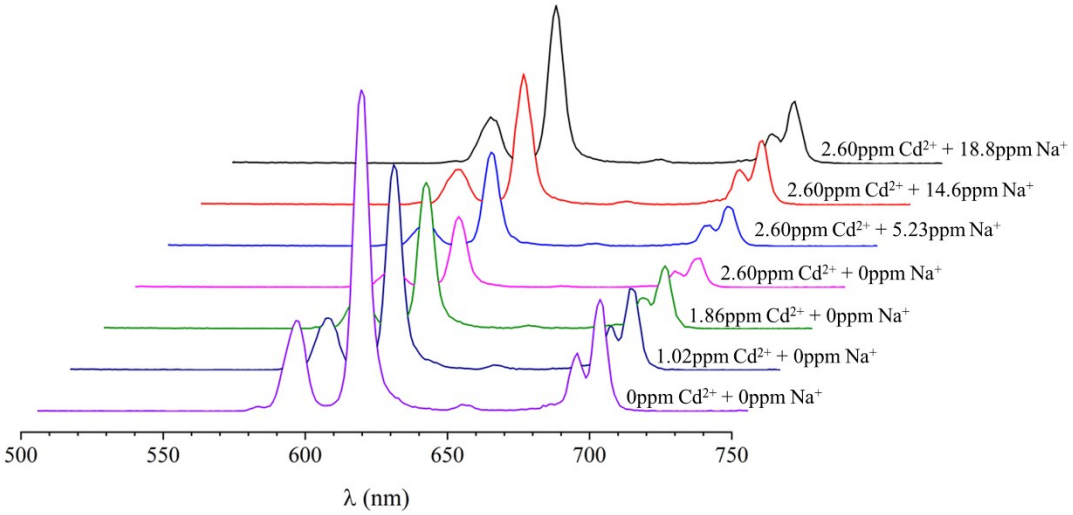

Figure S31. Luminescence spectra of Na_2(**1**)($Y_{0.95}Eu_{0.05}$) after the addition of increments of aqueous solution of $CdCl_2$(0.1M) indicating the drop of the luminescence signal followed by saturated aqueous solution of NaCl resulting in the recovery of the luminescence signal.

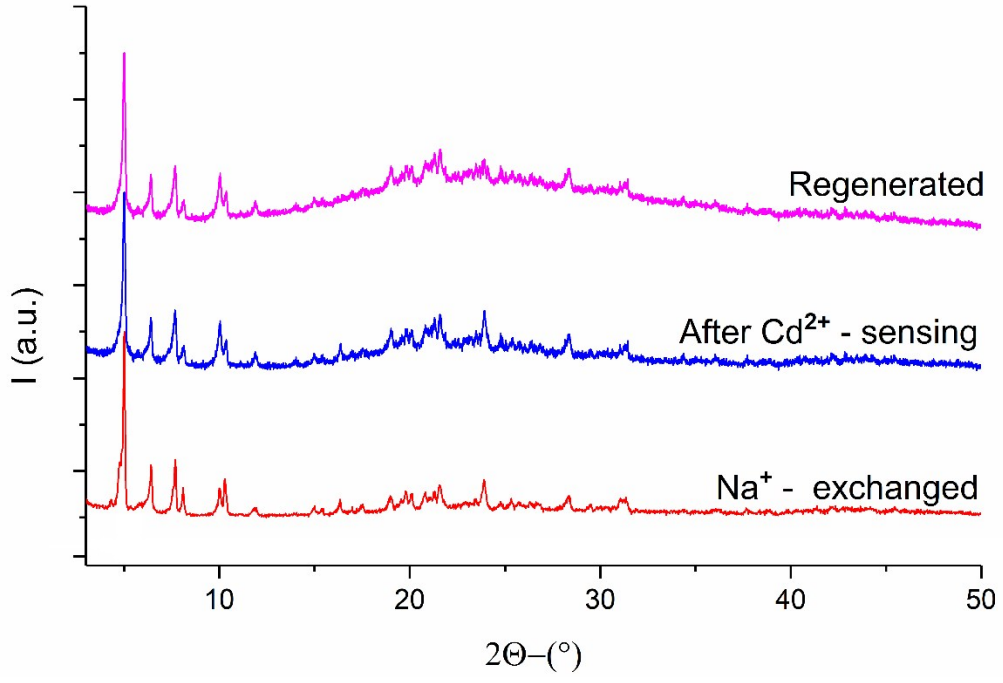

Figure S32. pXRD patterns of pristine Na_2(**1**)($Y_{0.95}Eu_{0.05}$), Cd^{2+} - exchanged Cd(**1**)($Y_{0.95}Eu_{0.05}$) i.e. the material isolated after Cd^{2+} sensing studies and Na^+ - exchanged Na_2(**1**)($Y_{0.95}Eu_{0.05}$) after regeneration experiment.

Cadmium Sorption Measurements

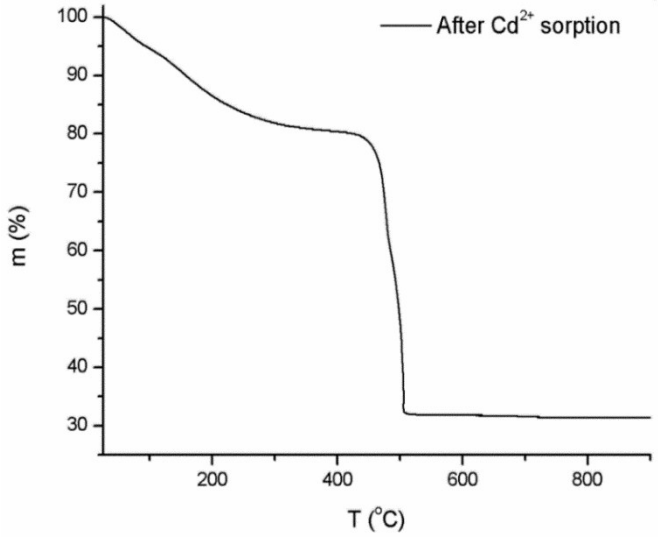

Figure S33. TGA graph of Cd^{2+}@(**1**)(Y) ((**1**)$(Y)^{2-}$ containing Cd^{2+} into its pores). TG analysis reveals that the thermal decomposition of compound Cd^{2+}@(**1**)(Y) proceeds via a two-step process. The first step (until ~430°C) is attributed to the removal of the lattice DMF molecules (observed: 20%, calculated: 20%). The second mass loss which is completed at ~520°C is attributed to the decomposition of the ligand OBA^{2-} (observed: 49%, calculated: 51%). Lastly the residual mass at 900°C corresponds to the mixed oxide of Y_2O_3 and 1.25CdO (observed: 31%, calculated: 29%).

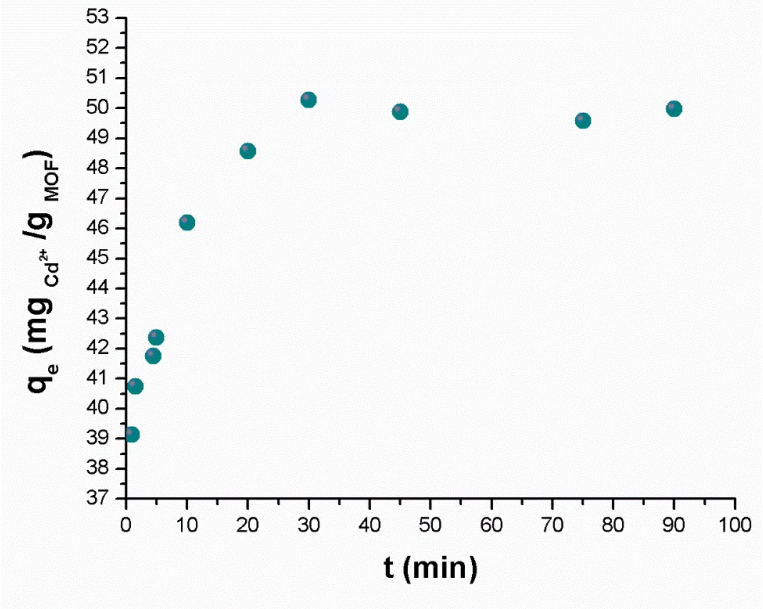

Figure S34. The kinetics of Cd^{2+} sorption by Na_2(**1**)(Y), C_{in} = 1 mM, $m_{sorbent}$: Na_2(**1**)(Y) = 0.066 g, $V_{solution}$ = 100 ml (70 ml DMF, 30 ml H_2O) and T = 296 ± 2 K.

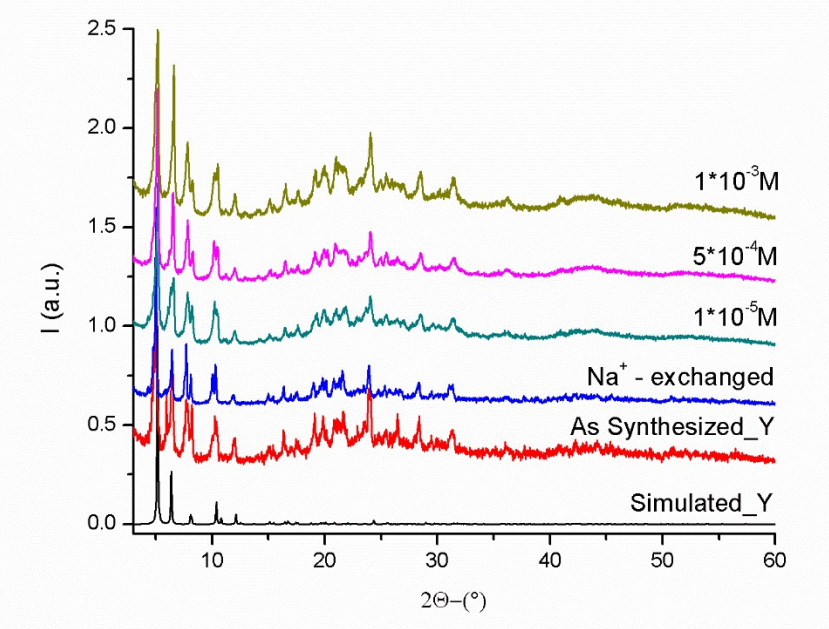

Figure S35. Powder X-ray diffraction patterns of Cd^{2+}@(**1**)(Y) ((**1**)$(Y)^{2-}$ containing Cd^{2+} into its pores); C_{in} = shown in the figure, aqueous DMF solution (30%), t = 120 min, $m_{sorbent}$: Na_2(**1**)(Y) = 0.033g, $V_{solution}$ = 30 ml and T = 296 ± 2 K.

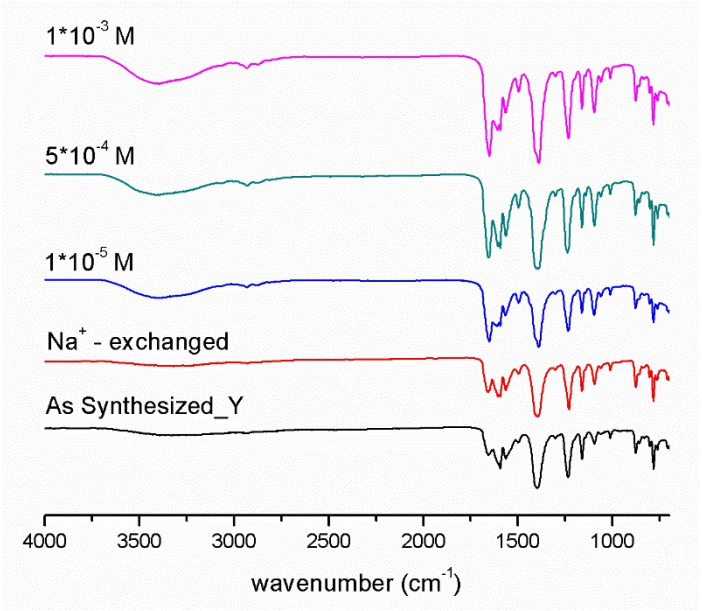

Figure S36. IR spectra of Cd^{2+}@(**1**)(Y) ((**1**)$(Y)^{2-}$ containing Cd^{2+} into its pores); C_{in} = shown in the figure, aqueous DMF solution (30%), t = 120 min, $m_{sorbent}$: Na_2(**1**)(Y) = 0.033g, $V_{solution}$ = 30 ml and T = 296 ± 2 K.

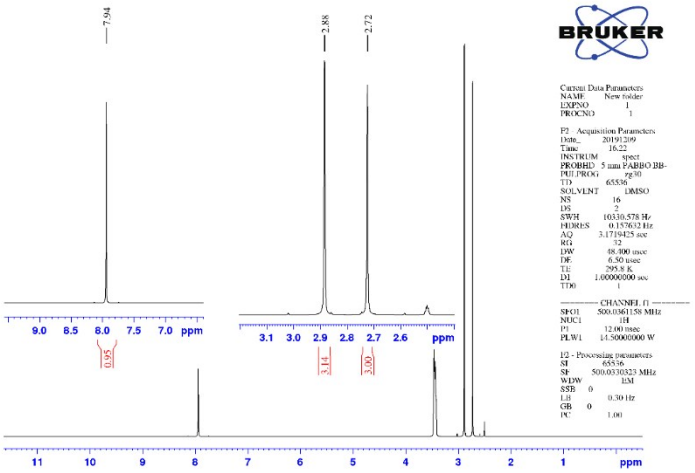

Figure S37. ^{1}H-NMR spectrum of the solution after Cd^{2+} sorption experiment in d_6-DMSO. $C_{in} = 5*10^{-4}$M, aqueous DMF solution (30%), t = 120 min, $m_{sorbent}$: Na_2(**1**)(Y) = 0.033g, $V_{solution}$ = 30 ml and T = 296 ± 2 K. These data indicate only the presence of DMF in (**1**)$(Y)^{2-}$ and the absence of organic ligand OBA^{2-} in the solution. Exact assignment DMF ^{1}H-NMR peaks is given in Figure S4.

Proposed structure of Cd^{2+}@(1)(Y) and Mg^{2+}@(1)(Y) based on powder X-ray diffraction data

Several powder X-ray diffraction patterns were collected with 0.01 º step and 2 sec exposure time on samples belonging to the same batch of Cd^{2+}@(**1**)(Y) and Mg^{2+}@(**1**)(Y). The patterns were smoothed and their background was subtracted separately, and then were merged using the WinPLOTR[11] software. The resulting pattern was introduced to EXPO2014[12], where indexing with implemented N-TREOR09[13] was performed. This, for Cd^{2+}@(**1**)(Y), led to a trigonal cell slightly different from that of the pristine material obtained from single crystal data. Le Bail refinement led to unit cell parameters $a = b = 27.579$ Å, $c = 26.221$ Å, $\alpha = \beta = 90$ and $\gamma = 120$ º (angles were fixed). (Fig. S37)

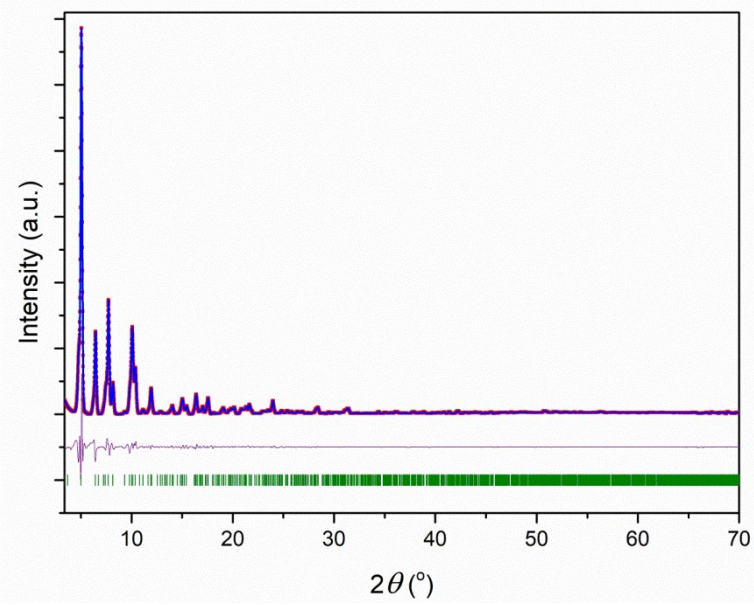

Figure S38. Le Bail refinement of Cd^{2+}@(**1**)(Y). Rp = 9.89, Rwp = 15.75. Red squares: observed pattern; blue line: calculated pattern; purple line: difference; green bars: observed reflections markers.

These parameters were used to replace the original cell dimensions of the pristine material, and after the reduction of the symmetry (space group was transformed from R-3 to P3), two ideal $[Cd(H_2O)_6]^{2+}$ octahedra with half occupancy (to balance the charge of the network) were placed in the cell at random positions. The transformations did not lead to significant modifications of the geometrical characteristics of the molecular structure of the anionic network. Simulated annealing with EXPO14 was used to solve the structure allowing only the $[Cd(H_2O)_6]^{2+}$ cations to move. The common characteristic of the derived solutions was the octahedral cation being positioned in close proximity to the etheric oxygen atoms of the OBA^{2-} ligand (Fig. S33).

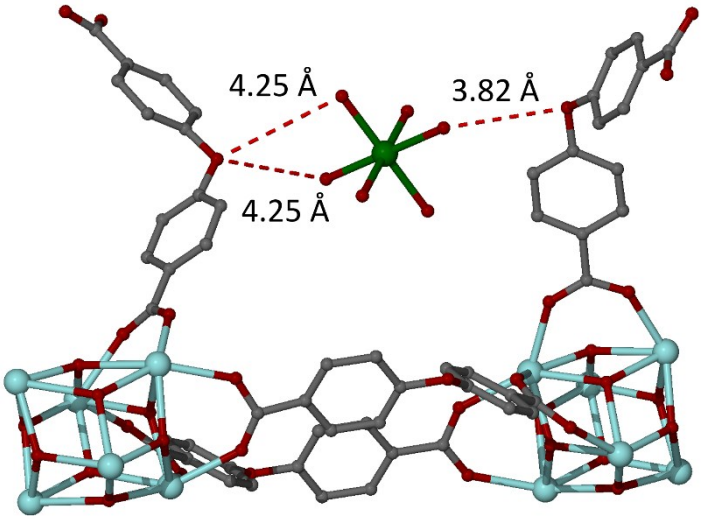

Figure S39. The location of $[Cd(H_2O)_6]^{2+}$ cations as derived by the simulated annealing structure solution with EXPO14. The second $[Cd(H_2O)_6]^{2+}$ possess a very similar position between a different pair of OBA^{2-} ligands.

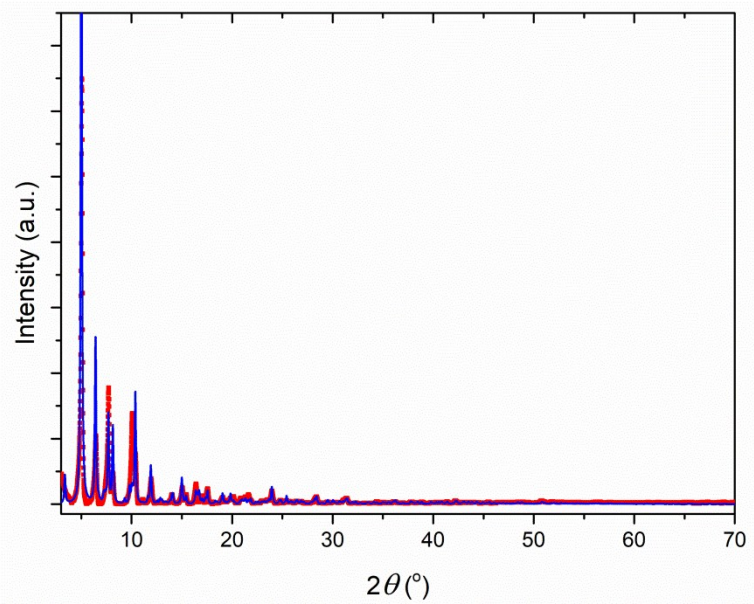

Figure S40. A comparison between the simulated powder XRD pattern from the structural model of the Cd^{2+} - exchanged material (blue line) with the experimental pattern (red squares).

The interaction of the cationic octahedron with the etheric oxygen can easily be realized when a second coordination sphere about the cation is considered. Although there is some crystallographic uncertainty concerning the obtained solution, we believe that the proposed model is realistic and chemically sound. There are several reasons to support this belief. a) The simulated X-ray pattern of the proposed structure is very similar to the experimental one (Fig.

S34). b) Very similar solutions were obtained when the symmetry of the initial model was increased changing the space group from P3 to P-3. c) The same procedure (i.e. collecting the powder X-ray patterns, processing, indexing, Le Bail refinement and solving the structure with simulated annealing) was applied for the Mg^{2+} - exchanged material leading to a similar structure solution involving a $[Mg(H_2O)_6]^{2+}$ octahedron in close proximity to the etheric oxygen atoms. (Figs. S35 – S37)

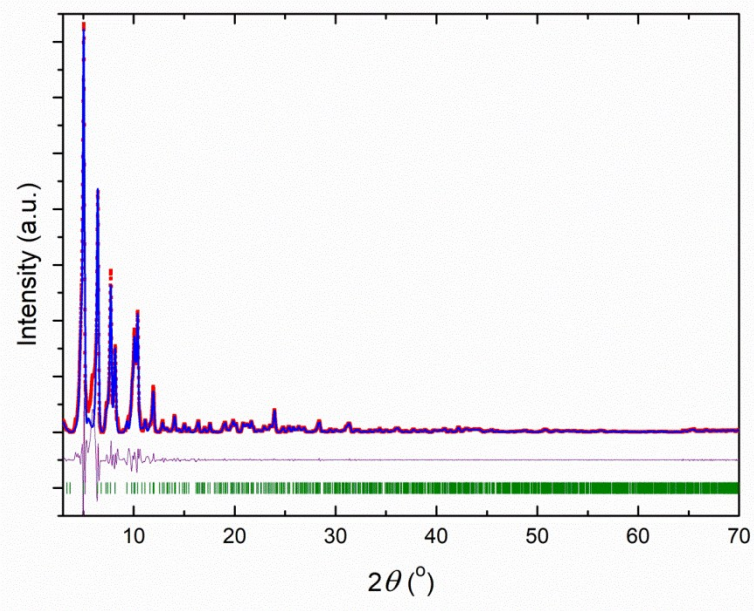

Figure S41. Le Bail refinement of the Mg^{2+} - exchanged material. Cell dimensions: $a = b =$ 27.551 Å, c = 26.147 Å, $\alpha = \beta = 90$ and $\gamma = 120$ °. Rp = 15.36, Rwp = 25.60. Red squares: observed pattern; blue line: calculated pattern; purple line: difference; green bars: observed reflections markers.

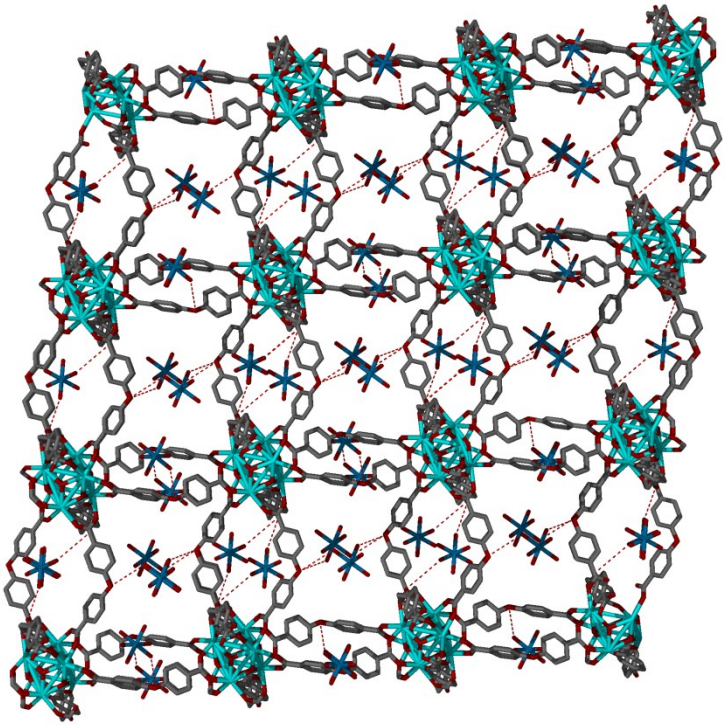

Figure S42. A packing diagram down to the (-1, -2, 1) cell dimension of the structural model produced for the Mg^{2+} - exchanged material with simulated annealing structure solution using EXPO14. Dashed red lines represent interactions similar to those presented in Fig. S33.

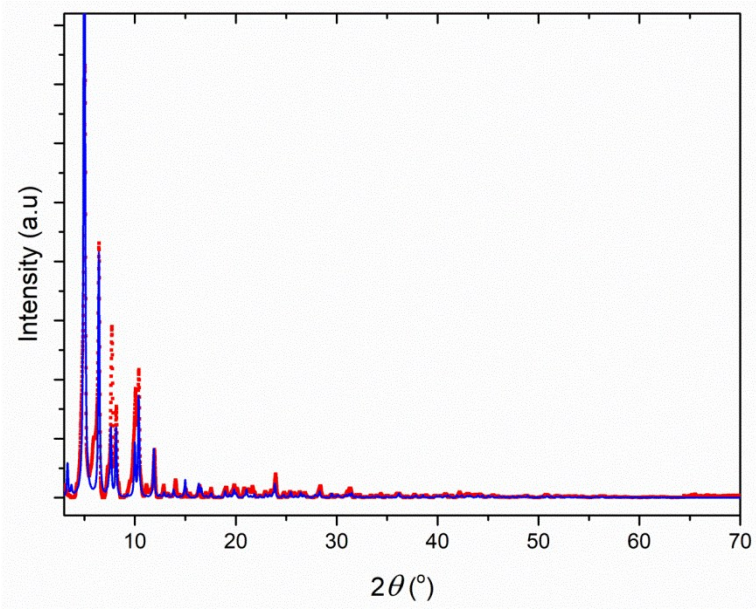

Figure S43. A comparison between the simulated powder XRD pattern from the structural model of the Mg^{2+} - exchanged material (blue line) with the experimental pattern (red squares).

References

1 G. Sheldrick, *Acta Crystallogr. Sect. A*, 2008, **64**, 112–122.

2 E. OxfordDiffraction, CrysAlis CCD and CrysAlis RED, version p171.38.46; Oxford Diffraction Ltd, Abingdon, Oxford, *No Title*, 2017.

3 L. J. Farrugia, *J. Appl. Crystallogr.*, 1999, **32**, 837–838.

4 K. Brandenburg, *DIAMOND*, 2014, Version 3.2k, Crystal Impact GbR, Bonn, Germany.

5 A. Spek, *J. Appl. Crystallogr.*, 2003, **36**, 7–13.

6 L. Czepirski and J. JagieŁŁo, *Chem. Eng. Sci.*, 1989, **44**, 797–801.

7 K. Sumida, D. L. Rogow, J. A. Mason, T. M. McDonald, E. D. Bloch, Z. R. Herm, T.-H. Bae and J. R. Long, *Chem. Rev.*, 2012, **112**, 724–781.

8 A. L. Myers and J. M. Prausnitz, *AIChE J.*, 1965, **11**, 121–127.

9 Y.-S. Bae, K. L. Mulfort, H. Frost, P. Ryan, S. Punnathanam, L. J. Broadbelt, J. T. Hupp and R. Q. Snurr, *Langmuir*, 2008, **24**, 8592–8598.

10 G. S. Armatas and M. G. Kanatzidis, *Nat. Mater.*, 2009, **8**, 217.

11 WinPLOTR: a Windows tool for powder diffraction patterns analysis. T. Roisnel, J. Rodriguez-Carvajal, in Materials Science Forum, Proceedings of the Seventh European Powder Diffraction Conference (EPDIC 7), 2000, p.118-123, Ed. R. Delhez and E.J. Mittenmeijer.

12 A. Altomare, C. Cuocci, C. Giacovazzo, A. Moliterni, R. Rizzi, N. Corriero and A. Falcicchio, *J. Appl. Crystallogr.*, 2013, **46**, 1231–1235.

13 A. Altomare, G. Campi, C. Cuocci, L. Eriksson, C. Giacovazzo, A. Moliterni, R. Rizzi and P.-E. Werner, *J. Appl. Crystallogr.*, 2009, **42**, 768–775.